Journal of Volcanology and Geothermal Research 387 (2019) 106663

Contents lists available at ScienceDirect

Journal of Volcanology and Geothermal Research

journal homepage: www.elsevier.com/locate/jvolgeores

Hot spring hydrochemistry of the Rio Grande rift in northern New Mexico reveals a distal geochemical connection between Valles Caldera and Ojo Caliente

Valerie J. Blomgren [a,*], Laura J. Crossey [a], Karl E. Karlstrom [a], Tobias P. Fischer [a], Thomas H. Darrah [b]

[a] Earth and Planetary Sciences Department, University of New Mexico, Northrop Hall 221 Yale Blvd NE, Albuquerque 87131, NM, USA
[b] School of Earth Sciences, The Ohio State University, Columbus, OH, 43210, USA

ARTICLE INFO

Article history:
Received 25 November 2018
Received in revised form 13 August 2019
Accepted 16 August 2019
Available online 20 August 2019

Keywords:
Chemistry
Carbon isotopes
Geothermal
Helium isotopes
Hot springs

ABSTRACT

Warm and hot springs occur within and on both sides of the Rio Grande rift (RGR) of northern New Mexico. Springs on the western side of the RGR are along the Ojo Caliente fault zone, which intersects the Embudo fault transfer zone that extends northeast of the Valles Caldera. Springs on the eastern side occur along north-south rift-bounding faults near Taos, NM. We compared spring water geochemical data from the western and eastern sides of the RGR to discover spring water origins. Included in our discussion was spring chemistry of the Valles Caldera located to the southwest of our study area. The Valles Caldera is a significant feature because it had major rhyolite eruptions 1.65 and 1.26 Ma, continued rhyolite eruptions until ~30 ka, and an active magmatically-driven geothermal system. The latest volcanic events in the Taos Plateau were basalt flows occurring about ~ 2 Ma. Our spring chemistry findings showed elevated levels of geothermal input in the western spring group, with the greatest input in Ojo Caliente spring waters. The elevated geothermal tracers include CO_2, Li, B, Na, Cl, HCO_3, C_{ext}, He, Sr, mantle-like $\delta^{13}C$-CO_2 values (−3.5 to −6.8‰), radiogenic basement-like $^{87}Sr/^{86}Sr$ ratios (0.747), and mantle-derived ^{3}He (up to 4.8%) in the presence of highly elevated crustal ^{4}He. Eastern springs had fewer magmatic inputs including tracers listed above and notably lower $^{87}Sr/^{86}Sr$ ratios ranging from 0.708 to 0.713. Nevertheless, eastern springs contain endogenic carbon and helium isotope values showing up to 4% mantle-derived helium. We interpret the elevated tracer results discovered in Ojo Caliente spring waters as distal influences of the Valles geothermal system, which is about 60 km away. The most conclusive evidence for these results stem from significant contributions of magmatically-derived volatiles including CO_2, He, and their isotopes. With evidence of far-traveled water and volatiles, we concluded that the RGR transfer zone fault systems provide conduits for long-distance migration of deep fluids and gases that mix with meteoric water in the shallow subsurface.

1. Introduction and motivation

Geothermal systems often involve mixing between epigenic (shallow/meteoric) water and endogenic (deeply sourced/geothermal) fluid derived from below the regional aquifer (Crossey et al., 2016). Our aim is to identify small-volume contributions of geochemically potent endogenic fluid mixing with larger volumes of meteoric water. To this end, we studied fluid mixing of various origins using a multi-tracer chemical approach. Volatile (e.g. noble gases, CO_2 and their isotopes) and hydrochemical (e.g., Li, B, Na, Cl, HCO_3, $^{87}Sr/^{86}Sr$) analyses constrain fluid origins, fluid transport pathways, and gas-water-rock interactions occurring in geothermal systems (Ellis and Mahon, 1977; Shaw et al., 2003; Evans et al., 2006; Tassi et al., 2010; Barry et al., 2014).

Noble gases are commonly used for evaluating the evolution of hydrothermal and magmatic systems as well as distinguishing the source, mixtures, and sub-surface crustal interactions of mantle-derived fluids, because of their inert nature, low abundances, and well-characterized isotopic compositions for each major terrestrial reservoir (i.e., mantle, crust, hydrosphere, and atmosphere) (Clarke et al., 1969; Lupton et al., 1977; Poreda and Craig, 1989; Sherwood Lollar et al., 1997; Polyak et al., 2000; Ballentine et al., 2002; Gilfillan et al., 2008; Tedesco et al., 2010; Darrah et al., 2013; Barry et al., 2014). Helium isotope analysis is particularly important for hydrothermal and magmatic studies in continental settings, because even small contributions of mantle-derived helium are resolvable

Abbreviations: (RGR), Rio Grande Rift.

* Corresponding author.
E-mail addresses: valerie.blomgren@gmail.com (V.J. Blomgren), lcrossey@unm.edu (L.J. Crossey), kek1@unm.edu (K.E. Karlstrom), fischer@unm.edu (T.P. Fischer), darrah.24@osu.edu (T.H. Darrah).

https://doi.org/10.1016/j.jvolgeores.2019.106663
0377-0273/

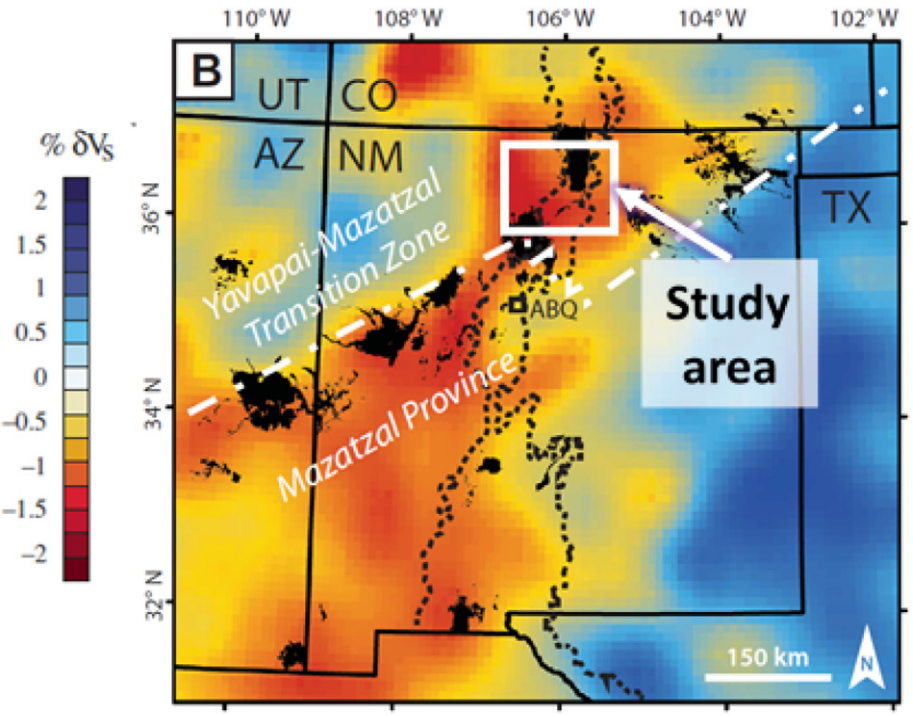

Fig. 1. Mantle tomographic image at 80 km depth in New Mexico from Schmandt and Humphreys (2010). The study area is located in north-central New Mexico at the intersection of the RGR and the Jemez lineament. The RGR is shown by the black dotted lines trending north-south and is characterized by a series of half grabens. The Jemez lineament is shown as black basalt fields located along the Yavapai-Mazatzal transition zone, which is represented by the dashed white line (Nereson et al., 2013). The coloring represents mantle velocity, orange/red = low velocity and blue = high velocity shown in ‰δV_s (Schmandt and Humphreys, 2010). Slow mantle velocity domains contain partial melt, are warmer and more buoyant.

and quantifiable in mixed crustal fluids (Ballentine et al., 2002; Crossey et al., 2006, 2009, 2011; Karlstrom et al., 2013; Crossey et al., 2016).

The migration of fluid and gases is possible in part because of preferential pathways along fault zones (Mailloux et al., 1999; Johnson et al., 2013; Fischer and Chiodini, 2015). Furthermore, fault zones are significant in areas of extension, crustal thinning, high geothermal gradient, and magmatic systems because they allow the relatively rapid ascent of geothermal waters (Kennedy and van Soest, 2007; Easley et al., 2011; Easley and Morgan, 2013; Karlstrom et al., 2013; Crossey et al., 2016; Lee et al., 2016). In our study area, the impact of faulting in regions underlain by low mantle velocity and young magmatism (Steck et al., 1998; Schmandt and Humphreys, 2010) is apparent because of mantle helium discovered in local spring water (Newell et al., 2005; Crossey et al., 2016). Similarly, carbonic springs with P_{CO2} values much higher than atmospheric levels ($10^{-3.5}$) are present and are considered a manifestation of deeply derived fluids (Newell et al., 2005; Crossey et al., 2006, 2009, 2011; Easley and Morgan, 2013; Karlstrom et al., 2013). These findings demonstrate the importance of studying spring fluid and gas chemistry in northern New Mexico to better understand the relationship of geothermal settings, tectonics, and fluid migration.

In this contribution, we address two questions. 1) Do springs on opposite sides of Rio Grande rift (RGR) have different chemistries? 2) For the western spring group, what are the influences of the modern Valles Caldera geothermal system, and are the Embudo and Ojo Caliente faults possible conduits for fluid and gas migration?

2. Regional setting

2.1. Structural and tectonic settings

The study area is located at the intersection of the RGR and the Jemez lineament (Fig. 1), an area defined by thin crust, slow mantle velocities, and a young volcanic history (Goff and Janik, 2002; Schmandt and Humphreys, 2010; Zimmerer et al., 2016). This tectonic setting motivates the study of volatile degassing into spring water and the relationship of water chemistry and spring locations to the RGR and Jemez lineament faults. The Jemez lineament is a northeast-trending zone of volcanoes that transects New Mexico, extending from Arizona through the Taos Plateau to the Raton-Clayton volcanic field on the Great Plains (Nereson et al., 2013). The southern edge of the Jemez lineament is coincident with the Proterozoic Yavapai and Mazatzal suture zones (Magnani et al., 2004), and is theorized to have been reactivated as a conduit for magma ascent in the late Cenozoic (Fig. 1) (Nereson et al., 2013).

The RGR is a north-south trending series of asymmetrical half grabens (extensional basins), with a dominant normal fault on one side and a hinge or zone of smaller displacement faults on the other (Koning et al., 2004). Our study site involves two RGR basins, the San Luis Basin to the north and Española Basin to the south (Fig. 2). The San Luis Basin is bordered to the east by the west-dipping Sangre de Cristo fault that has 7–8 km of displacement locally (Fig. 3) (Lipman and Mehnert, 1979), which causes asymmetric subsidence of the basin (Bauer and Kelson, 2004). The Española Basin is west-tilted because of greater displacement along the Santa Clara-Pajarito fault system (Koning et al., 2013).

The Embudo fault system is part of a northeast-southwest trending accommodation zone that transfers displacement between the master faults of the San Luis and Española Basins allowing for differential subsidence (Fig. 2) (Muehlberger, 1979). It also aligns with the central graben of the Valles Caldera system (Goff et al., 2011) suggesting that the location of this felsic caldera system was influenced by pre-existing structures. The Embudo fault is predominantly a left lateral strike slip fault with minor north-down dip slip motion (Bauer and Kelson, 2004) (Fig. 2). At larger scale, this fault system also provides a surface

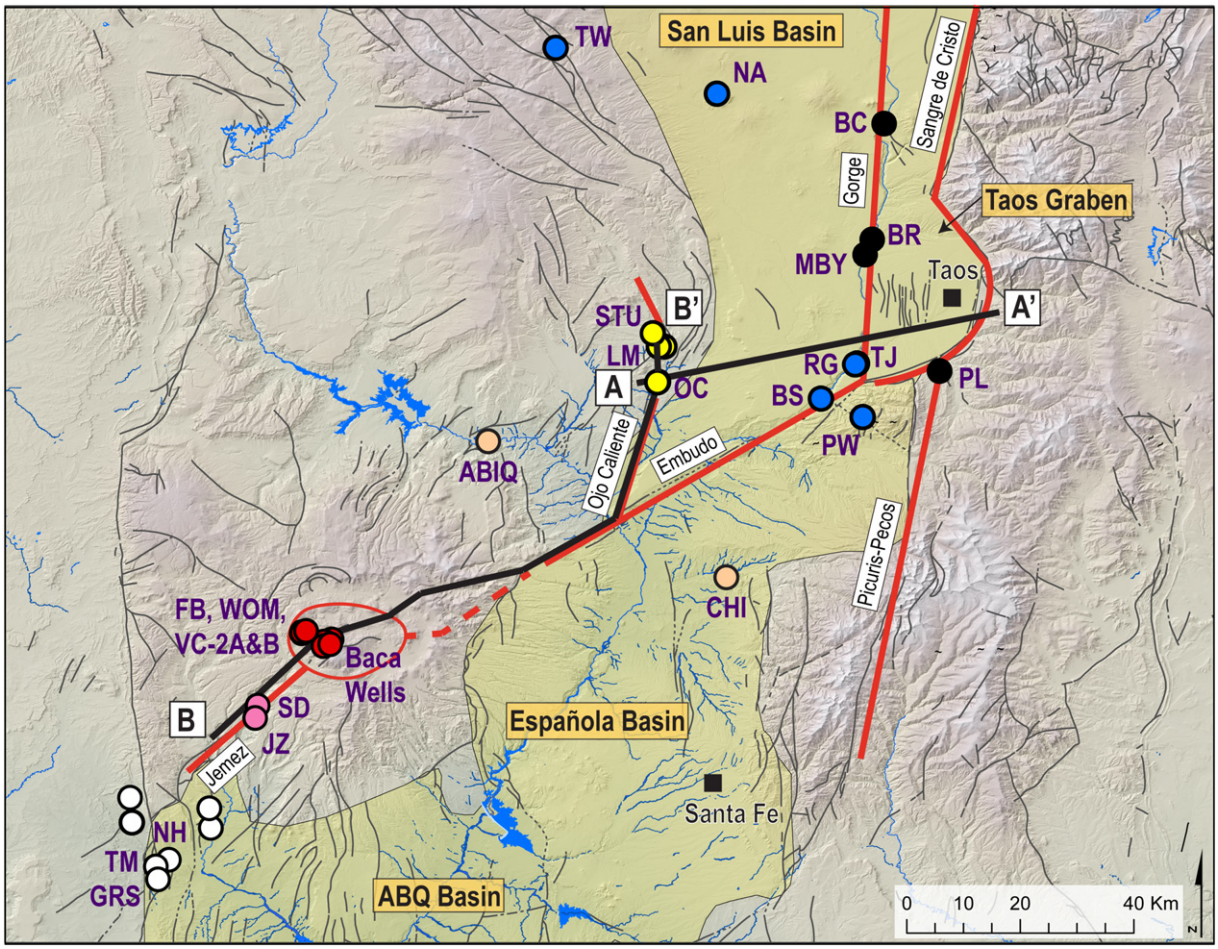

Fig. 2. Study Area showing Valles Caldera and springs. The base map shows topography and regional faults (from the New Mexico Bureau of Mines and Mineral Resources). The red bold lines show the dominant faults associated with springs of this and related studies. The shaded area trending north-south is the RGR composed of the San Luis, Española and Albuquerque (ABQ) basins. The bold black lines are cross section lines. The symbol colors represent different spring groups. Yellow symbols = western RGR springs; black = eastern RGR springs; blue = meteoric springs; red = Valles Caldera springs; pink = geothermal outflow plume of the Valles Caldera; white = Tierra Amarilla and Penasco springs; peach = other regional springs northeast of the Valles Caldera. Abbreviations for the springs are presented in Table 1 and listed here: Abiquiú spring (ABIQ), Baca wells (B13, B15, B24, B4), Bear Crossing (BC), Big spring (BS), Black Rock (BR), Chimayó (CHI), Footbath (FB), Grassy spring (GRS), Jemez spring (JZ), La Madera (LM), Manby (MBY), No Agua well (NA), North Highway (NH), Ojo Caliente (OC), Picuris Warm spring (PW), Ponce de Leon (PL), Rio Grande spring (RG), Soda Dam (SD), Statue (STU), Taos Junction (TJ), Tusas Warm spring (TW), Twin Mounds (TM), Valles Caldera wells (VC-2A and VC-2B), and Women's Bath (WOM).

expression of the Jemez lineament (Muehlberger, 1979) and is aligned with the northeast-southwest trending zone of low mantle velocity seen in Fig. 1.

Within the east-central part of the San Luis Basin is the north-south trending Taos Graben (Fig. 2) that is bordered to the east by the Sangre de Cristo fault and on the west by the buried east-dipping Gorge fault (Bauer and Kelson, 2004). Grauch and Keller (2004) imaged the Gorge fault 17 km north of Questa, NM and as far south as Taos, NM. The graben deepens to the south of Taos and is inferred to continue south intersecting with the Embudo fault (Grauch and Keller, 2004). The Taos Graben was also imaged with gravity data in Cordell (1978). The Gorge fault hosts the majority of the hot springs in the eastern spring group: Bear Crossing, Manby, and Black Rock. Bear Crossing spring is located at the intersection of the Gorge and Red River faults near Questa, NM, (Johnson and Bauer, 2012). The final spring of the eastern spring group is Ponce de Leon located near the intersection of the Embudo and Picuris-Pecos faults. The Picuris-Pecos fault was formed in the Proterozoic, reactivated during the Laramide orogeny (Miller et al., 1963), and had further displacement in the Neogene as a rift normal fault (Bauer and Kelson, 2004).

The Embudo fault is present on the western side of the RGR and intersects the northwest-dipping Ojo Caliente fault zone (Koning et al., 2011), which hosts the western springs of this study: Ojo Caliente, La Madera, and Statue (Fig. 2). The Ojo Caliente fault zone is extensional and offsets Proterozoic bedrock against Tertiary Santa Fe Group with related faults bounding Quaternary travertine (Crossey et al., 2011). Springs and vents are presently discharging along the Ojo Caliente fault system suggesting the faults are tectonically active. The springs have high concentrations of dissolved CO_2 causing travertine deposition. By dating the travertine with uranium-series, Crossey et al. (2011) showed that the springs have been discharging water for >100–200 thousand years.

2.2. Magmatic setting

The volcanic system near the western part of the study area is known as the Jemez volcanic field. The eastern volcanic rocks are part of the Taos Plateau volcanic field. Both are part of the Jemez volcanic lineament and overlie low velocity mantle but their volcanic histories differ. The Jemez volcanic system developed over the last 16 Ma (Gardner and Goff, 1984; Zimmerer et al., 2016) and culminated with two supervolcano caldera-style rhyolitic ash flow tuff eruptions at 1.65 and 1.26 Ma (Spell et al., 1996; Goff et al., 2014; Zimmerer et al., 2016). The youngest Jemez volcanism was the 68 ka Banco Bonito and 74 ka El Cajete rhyolitic

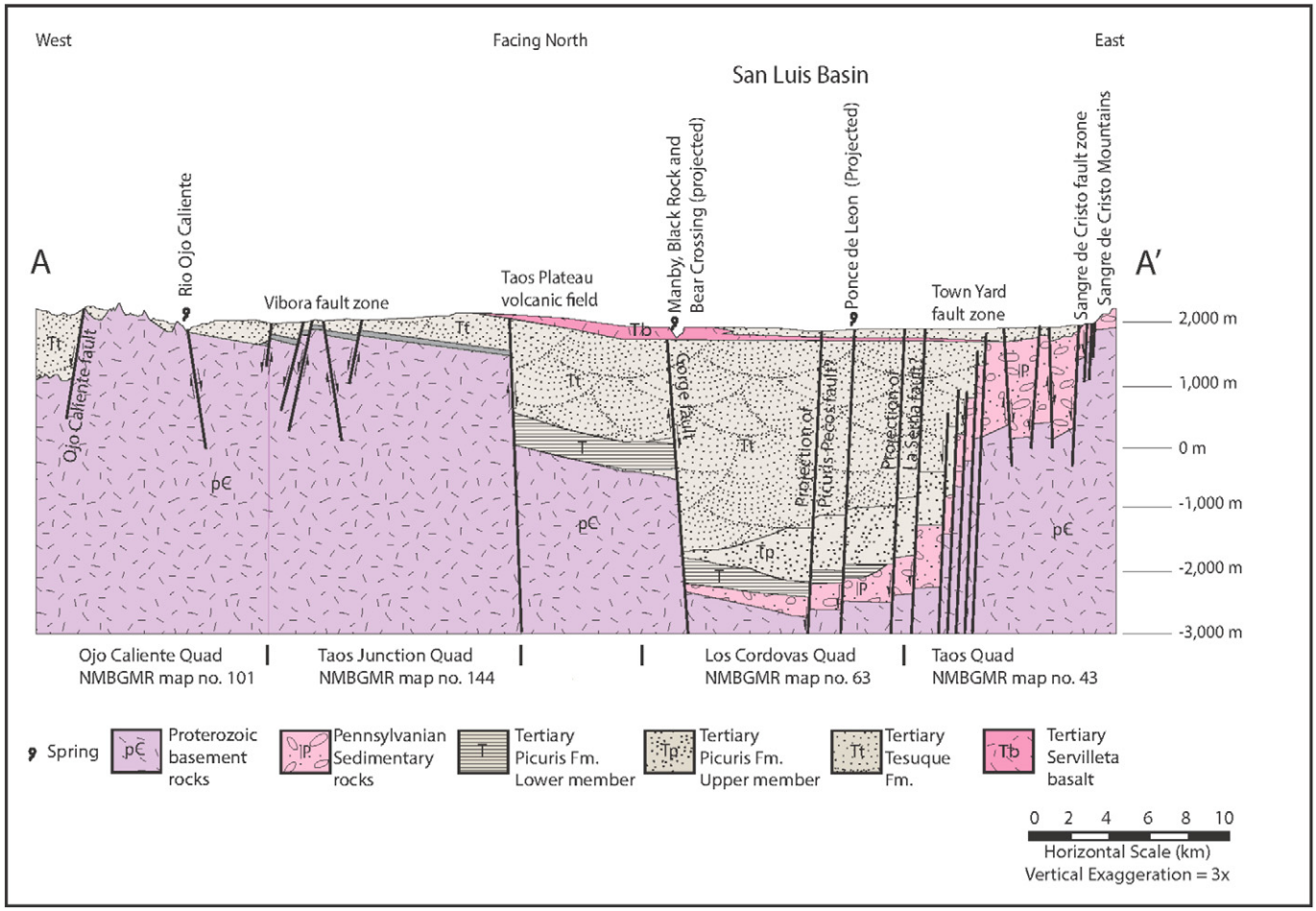

Fig. 3. West-east cross section of the southern San Luis Basin from Ojo Caliente to the base of the Sangre de Cristo Mountains (modified from Bauer and Kelson, 2004 and New Mexico Bureau quadrangle maps listed in the figure). Basement normal faults are located on either side of the RGR, which motivates the study of deep volatiles ascending along the faults. The Gorge fault and Picuris-Pecos faults are both projected into the cross section. The former is an eastern rift-bounding fault and has greater displacement than the western rift-bounding faults, reflecting the half-graben basin geometry that is present throughout the RGR. The RGR fill is Tertiary sediment of the Santa Fe Group overlain by basalt flows.

flows and pumice deposits (Zimmerer et al., 2016). The Taos Plateau volcanism ranges from 2 to 6 Ma (Lipman and Mehnert, 1979; Appelt, 1998; Repasch et al., 2017) and was dominantly mafic to intermediate in composition (basalt, andesite, and dacite) although rhyolitic volcanos are also found in the region (Johnson and Bauer, 2012).

The Valles Caldera hosts a magma-driven geothermal system (Goff and Gardner, 1994). Nielson and Hulen (1984) estimated the top of the magma body at 4.7 km below the ground surface, and Aprea et al. (2002) imaged the magma body with seismic data at 7 ± 1 km below the ground surface. The gases and solutes of the Valles Caldera geothermal system were characterized in Truesdell and Janik (1986), Vuataz et al. (1988), and Goff and Janik (2002), which reported mantle helium signatures as high as 6 RA (Goff and Janik, 2002). Regional influence of the Valles Caldera geothermal system includes a plume of geothermal water flowing laterally from the Caldera southwest along the Jemez fault (Fig. 2) (Goff and Gardner, 1994), and distal expressions found further southwest along the San Diego Canyon fault, 42–48 km, to Tierra Amarillo springs (McGibbon et al., 2018). These distal expressions are similar to our work presented here.

2.3. Regional aquifers

The main aquifer of the study area is the Santa Fe Group (Drakos et al., 2004) deposited from the early Miocene to about 1 Ma. The oldest layer of the Santa Fe Group is the Tesuque Formation composed of the older Chama El Rito Member, an interbedded conglomerate and sandstone, and the younger Ojo Caliente Member, a fine to very fine, well-sorted aeolian sandstone. The next layer above is the Chamita Formation, a moderate to poorly sorted sandstone. The aquifer on the western side of the RGR is mainly composed of the Ojo Caliente Member and the Chamita Formation (Koning et al., 2011). The youngest layer of the Santa Fe Group is the Servilleta Formation, characterized as sediment interbedded with basalt flows (Drakos et al., 2004). The Servilleta Formation is shallow aquifer of the Taos Plateau and groundwater mainly flows in the sediment layers and within basalt fractures (Johnson and Bauer, 2012).

2.4. Using a multiple tracer approach

This study used multiple tracer analyses to develop two and three end-member mixing models capable of resolving deep end member volatile and fluid components (Crossey et al., 2009). The mixing trends extend from known meteoric values to empirically approximate endogenic end members. The types of tracers used include analytical, isotopic, and gas chemistry.

For analytical chemistry we studied major ions and presented the data in a Piper diagram to identify water-rock interactions and fluid mixing (Piper, 1944). Lithium and boron were studied because they

Table 1
Spring abbreviations, locations and parameters.

Sample name	Abbr.	Sample date	Elev. (m)	Latitude	Longitude	Temp (°C)	Depth (m)	pH	Cond. (μS)	TDS (ppm)	[b]Spec. cond. (μS)
Western Rio Grande rift springs											
La Madera Mother spring (a)	LM1	01/04/15	2029	36.361000	−106.041930	25.4	Surface	6.02	1610	805	1850
La Madera Mother spring (a)	LM1	06/20/15	2029	36.361000	−106.041930	25.9	Surface	5.77	1686	843	1739
La Madera pool (a)	LM2	01/04/15	1963	36.360990	−106.050700	24.5	Surface	6.32	1250	614	1784
La Madera pool (a)	LM2	06/20/15	1963	36.360990	−106.050700	26.1	Surface	6.07	1773	886	1896
Ojo Caliente Well (a)	OC-W	01/04/15	1908	36.305492	−106.051980	53.2	26[a]	6.63	3350	1700	6699
Ojo Caliente Lithium spring (a)	OC-L	01/04/15	1908	36.304573	−106.052953	41.7	Surface	6.68	3150	1810	5391
Ojo Caliente Iron spring (a)	OC-I	01/04/15	1908	36.304346	−106.053002	40.6	Surface	6.62	4240	2110	5397
Statue spring (a)	STU	01/05/15	2063	36.382080	−106.060130	25.0	Surface	6.34	1582	790	1662
Statue spring (a)	STU	06/20/15	2063	36.382080	−106.060130	28.5	Surface	5.78	1598	800	1789
Eastern Rio Grande rift springs											
Black Rock spring (a)	BR	01/06/15	1993	36.530668	−105.712160	38.3	Surface	7.61	810	405	1106
Manby spring (a)	MBY	06/06/15	NM	36.506748	−105.723633	38.5	Surface	7.0	788	394	1005
Bear Crossing spring (a)	BC	06/06/15	NM	36.714430	−105.693300	16.8	Surface	7.69	232	116	179
Ponce de Leon spring (a)	PL	01/06/15	2215	36.321998	−105.605657	33.0	Surface	8.60	769	384	989
Meteoric waters in study area											
Big spring (a)	BS	01/05/15	1861	36.278600	−105.793500	21.9	Surface	7.77	269	134	263
Taos Junction spring (a)	TJ	01/05/15	1851	36.334180	−105.736540	18.2	Surface	7.92	463	231	413
Rio Grande Spring (a)	RG	01/05/15	1871	36.332630	−105.739430	15.2	Surface	7.29	391	195	298
No Agua well (a)	NA	06/26/15	2333	36.761831	−105.958264	31.0	354	6.96	147	77.8	230
Tusas warm Spring (a)	TW	06/26/15	NM	36.834718	−106.214072	17.3	Surface	7.31	138	68	174
Picuris warm Spring (a)	PW	06/27/15	8104	36.249200	−105.727420	14.8	Surface	5.33	36.2	18.1	36
Valles Caldera springs and wells											
Footbath (b)	FB	1986–1998	NR	35.908045	−106.615599	20	Surface	1.10	NR	NR	NR
Women bath (b)	WOM	1993–1998	NR	35.906420	−106.616397	88	Surface	1.40	NR	NR	NR
Valles Caldera well VC-2A (b)	VC-2A	1987	NR	35.907595	−106.615534	210	NR	6.20	NR	NR	NR
Valles Caldera well VC-2B (b)	VC-2B	1989–1990	NR	35.910129	−106.609489	295	NR	4.74	NR	NR	NR
Baca well 13 (b)	B13	1974–1982	aprox. 2600	35.896512	−106.568831	289	2501	7.30	NR	NR	NR
Baca well 15 (b)	B15	1976–1982	aprox. 2600	35.893188	−106.580717	280	1673	7.12	NR	NR	NR
Baca well 24 (c)	B24	1981–1982	aprox. 2600	35.885825	−106.581993	260	3233	NR	NR	NR	NR
Baca well 4 (c)	B4	1973–1982	aprox. 2600	35.888989	−106.571063	295	1939	NR	NR	NR	NR
Valles Caldera SW geothermal outflow springs											
Soda Dam (b)	SD	1984–1994	NR	35.791681	−106.686041	47	Surface	NR	NR	NR	NR
Jemez spring (b)	JZ	1984–1992	NR	35.771981	−106.690110	75	Surface	NR	NR	NR	NR
Tierra Amarilla											
North Highway (e)	NH	6/30/2014	NR	35.547150	−106.826790	20.2	Surface	6.01	9430	4710	NR
Twin Mounds (e)	TM	6/30/2014	NR	35.536744	−106.847567	27.7	Surface	6.07	12,560	6370	NR
Grassy Spring (e)	GRS	6/30/2014	NR	35.516175	−106.843978	24.4	Surface	6.3	15,330	7600	NR

(a) this study; (b) Goff and Gardner, 1994; (c) Truesdell and Janik, 1986; (d) Goff and Janik, 2002; (e) Newell et al., 2005; McGibbon et al., 2018
NR - Not Reported.
NM - Not Measured.
[a] Well depth from Vuataz et al., 1984
[b] Specific conductance was modeled with PHREEQC Version 2.

can be associated with a thermal source and high temperature equilibration (Evans et al., 2006; Goff and Gardner, 1994). The elemental ratios, B/Cl and Li/Cl, were compared to geothermal fluids because these ratios do not equilibrate at lower temperatures (White et al., 1984), and therefore show mixing of reservoir and meteoric groundwater with preserved conservative components (Goff and Gardner, 1994). The Cl/Br ratio was reported because it signifies increased salinization due to geologic influence on groundwater (Phillips et al., 2003; Hogan et al., 2007; Williams et al., 2013). P_{CO2} was modeled with PHREEQC (Parkhurst, 1995), which expresses saturation of Ca, HCO_3 and CO_2. If P_{CO2} in water is higher than atmospheric levels of P_{CO2} ($10^{-3.5}$), then the water has more dissolved CO_2 compared to water equilibrated with the atmosphere, and therefore is an indicator of how much CO_2 will degas at spring vents (Drever, 1997).

Various isotopic chemical analyses were performed, beginning with the stable isotopes of hydrogen and oxygen used to identify evaporation and water-rock interaction trends relative to the Global Meteoric Water Line (GMWL) (Sharp, 2007). Carbon isotope analyses were used to distinguish among three sources of dissolved inorganic carbon (DIC): dissolved components of carbonates within an aquifer system (C_{carb}), organic volatiles from soil gas or plant respiration (C_{org}), and endogenic sources such as magmatic degassing or CO_2 from rising geothermal fluids from deep crust or mantle (C_{endo}) (Chiodini et al., 2004). Radiogenic strontium was analyzed because it reflects water-rock interaction along deep flow pathways through Precambrian granite and other types of rocks (Faure, 1986). An example of highly radiogenic Precambrian basement rock near our study area, that is generally similar in age and composition, is from the Rocky Mountain National Park in Colorado with an average $^{87}Sr/^{86}Sr$ value of 0.740 (Clow et al., 1997). In contrast, Paleozoic marine carbonates in New Mexico typically have an average $^{87}Sr/^{86}Sr$ ratio of 0.709 (Crossey et al., 2006).

For gas chemistry, we present Ar-N_2-He abundances on a trilinear diagram established by Giggenbach (1992). This diagram distinguishes among tectonic settings (rift and arc volcanic settings) and fluid sources (atmosphere and mantle). CH_4 was studied because abiotic CH_4 may be sourced from juvenile carbon from the mantle or high temperature synthesis reactions of CO_2 and H_2 (Welhan, 1988). Helium isotopes analyzed from dissolved gases were used to distinguish mantle and crustal components. Helium isotopes are reported as the term "R_C/R_A," which is the $^3He/^4He$ ratio normalized by the $^3He/^4He$ ratio of air

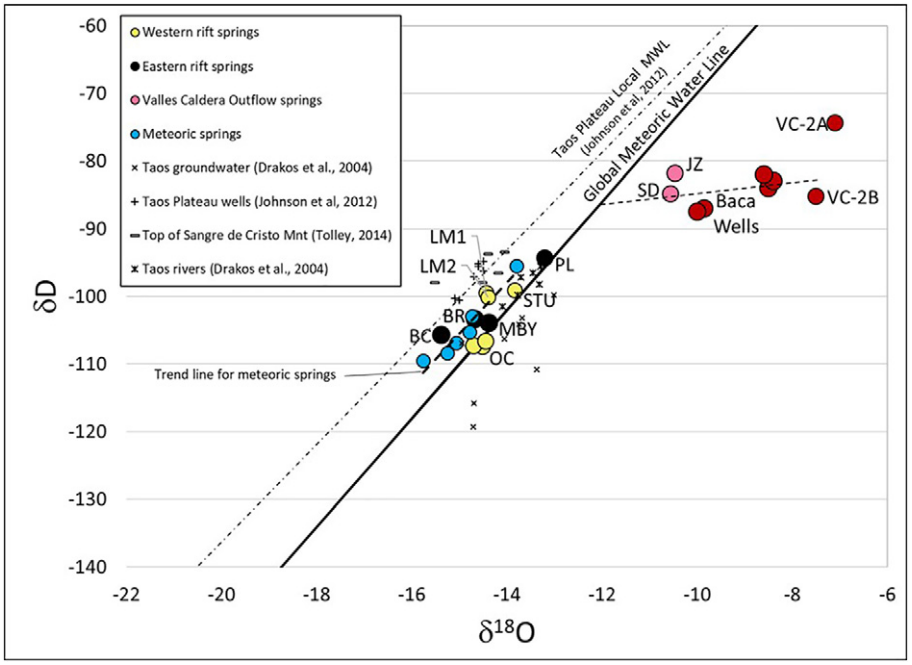

Fig. 4. Stable isotopes of hydrogen and oxygen. The stable isotopes of hydrogen and oxygen show how spring water samples compare to the Global Meteoric Water Line (GMWL), shown as a black line. Western and eastern spring water samples (yellow and black symbols, respectively) plot close to the GMWL showing the dominance of meteoric H_2O. Conversely, the Valles Caldera well samples (VC and Baca wells – red symbols) are a part of a geothermal system that underwent water-rock interaction seen as a roughly horizontal trend extending away from the GMWL (Goff and Gardner, 1994; Truesdell and Janik, 1986).

(Clarke et al., 1976) and corrected for air contamination (Hilton, 1996; Porcelli and Ballentine, 2002). The mantle contains the majority of the earth's ^{3}He compared to the crust, and radioactive decay processes in the crust produce significant amounts of ^{4}He that lowers the ^{3}He/^{4}He ratio in rising endogenic fluids (Ballentine et al., 2002). Fluids with less crustal influence have higher ^{3}He/^{4}He ratios. The fluids emanating from mid-ocean ridges have values of 8 ± 1 R_C/R_A (Poreda et al., 1992) and sources with no mantle input (i.e. in cratons) are below 0.02 R_C/R_A (Andrews, 1985). It is accepted that values of >0.1 R_C/R_A indicate a significant mantle-derived volatile component (Ballentine et al., 2002). In addition to R_C/R_A, the $CO_2/^3$He ratio is commonly studied because this ratio is well constrained for MORB fluids and increased ratios may reflect geothermal processes (Sano et al., 1988; Marty et al., 1989).

2.5. Significance of travertine

Travertine, commonly found in the study area, signifies a hydraulic connection between spring water and a subsurface reservoir of CO_2. Each mole of $CaCO_3$ deposited as travertine requires a mole of CO_2 to be degassed from the subsurface (Chafetz and Folk, 1984; Crossey et al., 2006, 2009). Furthermore, Priewisch et al. (2014) argued that travertine deposition in this area is facilitated by endogenic CO_2. The introduction of CO_2 in water causes limestone to dissolve increasing the concentration of Ca^{2+} and HCO_3^- ions in solution (Crossey et al., 2006). The species of dissolved inorganic carbon (e.g., H_2CO_3, HCO_3^-, CO_3^{2-}) is pH dependent. Neutral waters have dominantly HCO_3^-, aqueous CO_2 exists at low pH values (below ~5), and CO_3^{2-} exists at pH values above ~11 (Drever, 1997). Because the pH of samples collected in this study were all between 5 and 11, we focused on chemical equations using HCO_3^-. The chemical equations describing travertine deposition are shown in the mass balances below: 1) dissolution of limestone due to corrosive fluids with external CO_2 (C_{ext}) and 2) the deposition of travertine due to CO_2 degassing (Crossey et al., 2006).

$$\text{External } CO_{2(g)} + H_2O + CaCO_{3(\text{limestone})} \rightarrow Ca^{2+}{}_{(aq)} + 2HCO_3^-{}_{(aq)} \quad (1)$$

$$Ca^{2+}{}_{(aq)} + 2HCO_3^-{}_{(aq)} \rightarrow CO_{2(g)} + H_2O + CaCO_{3(\text{travertine})} \quad (2)$$

3. Methods

3.1. Sample collection

Spring water parameters were measured in the field for temperature, pH, and conductivity. Spring water was collected in two HDPE containers, one container was filled with filtered water and then acidified for cation analysis and the second container was unpreserved for anion and stable isotope analysis. Gas samples were collected in a Giggenbach bottle by inserting a hollow metal pole into the spring opening with plastic tubing connecting the pole to the Giggenbach bottle. The Ojo Caliente gas samples were collected in 12 mL glass vials with a rubber seal; gas collection was done by filling the vials with spring water and then displacing the spring water with gas bubbles (Cartwright et al., 2002). A subset of the samples, analyzed for noble gas isotopes, were collected in refrigeration-grade copper tubes sealed by cold welding with steel clamps. The copper tube method consisted of attaching plastic tubing on both ends of the copper tubing, then flushing the copper tube apparatus with approximately 50 volumes of spring water before clamping on both ends (Griesshaber et al., 1992; Newell et al., 2005).

3.2. Analytical methods

Stable isotopes of hydrogen and oxygen were analyzed using a Picarro WS-CRDS-based analyzer in the Center of Stable Isotopes at

the University of New Mexico (UNM). The Picarro had an evaporator system able to analyze liquid water for $H_2^{18}O$, $H_2^{16}O$ and $HD^{16}O$ (Gupta et al., 2009). The isotope results were referenced to Vienna Standard Mean Ocean Water (Sharp, 2007).

Major ion and trace element chemistry was analyzed in the Analytical Laboratory of the Department of Earth and Planetary Sciences of UNM. Alkalinity was determined by end point titration with sulfuric acid, anions were analyzed using the Dionex DX-500 ion chromatograph using EPA Method 300.1, Revision 1.0, (Hautman and Munch, 1997), and cations were analyzed using the Perkin Elmer Optima 5300DV inductively coupled plasma optical emission spectroscopy and the Perkin Elmer NexION 300 D mass spectrometer using EPA Method 200.7, Revision 4.4, (Martin et al., 1994).

Gas abundance analyses of He, H_2, Ar, N_2, O_2, CH_4, and CO was completed by using both a Gow-Mac series G-M 816 Gas Chromatograph (GC) and a Pfeiffer Quadrupole Mass Spectrometer (QMS) in the Volcanic Geothermal Fluid Analysis Laboratory at UNM. The relative abundances of CO_2, CH_4, H_2, Ar + O_2, N_2 and CO were measured with the GC using He as the carrier gas, and the relative abundances of He, Ar, O_2 and N_2 were measured in the QMS (Lee et al., 2016). The samples were connected to the GC and QMS with high vacuum lines that were designed to trap water in containers frozen with liquid nitrogen (Hilton, 1996).

Carbon isotopes were analyzed for water either collected in a HDPE bottle or copper tube, the container used for each sample is specified in Table 4. The carbon isotopes measured for water samples from HDPE bottles were analyzed in the Center of Stable Isotopes at UNM using the Finnigan Delta Plus isotope ratio mass spectrometer with a Finnigan MAT GasBench II. The procedure starts with adding the water sample to a vial under vacuum with a syringe, then adding phosphoric acid to cause a reaction with the water that produces CO_2 gas. The CO_2 gas is then carried to the mass spectrometer with helium as the carrier gas (Torres et al., 2005). Carbon isotopes measured for water samples from copper tubes were analyzed at the Rare Gas Laboratory at the University of Rochester, NY, using a Thermo Fisher Delta V IRMS, following methods from Darrah et al. (2013, 2014).

Strontium isotope analyses were performed in the Radiogenic Isotope Laboratory of UNM. Strontium was extracted from the water sample in a polypropylene column with strontium resin (product number LOT SRA 121517) described by De Muynck et al. (2009). First, the column was prepared by adding strontium resin and rinsing it with 3 N HNO_3 to remove matrix elements, for example Ca^{2+} and Rb^{+} (De Muynck et al., 2009). Then 18 MΩ H_2O was added to remove strontium from other sources. After the column was prepared, the spring water sample was added and rinsed with 3 N HNO_3 to remove matrix elements. Strontium was drained from the column by adding 18 MΩ H_2O and collected into a vial. The vial was then heated on a hot plate to evaporate water leaving behind dried strontium. The dried strontium was dissolved with 3%HNO_3 and analyzed in the ThermoFinnigan Neptune multiple collector ICP-MS (De Muynck et al., 2009; Ma et al., 2013).

Total helium concentration and the helium isotopic ratio ($^3He/^4He$) were analyzed at one of the following laboratories, the Noble Gas Laboratory at The Ohio State University, the Rare Gas Laboratory at the University of Rochester, or the Fluids and Volatiles Laboratory at Scripps Institution of Oceanography. The isotopic analyses were completed using the respective noble gas isotope ratio mass spectrometers and analytical techniques that have been described previously (Poreda and Farley (1992), Hilton (1996), Hunt et al. (2012), and Darrah et al. (2013, 2014)).

Table 2
Trace element concentrations (mg/L) and stable isotopes of hydrogen and oxygen.

Sample name	F	Br	Li	B	As	Cl/Br	$\delta^{18}O$ (‰)	δD (‰)
Western Rio Grande rift springs								
La Madera Mother spring (a)	1.63	0.30	0.28	0.48	BDL	339	−14.4	−99.5
La Madera Mother spring (a)	0.91	0.41	0.22	0.54	BDL	244	−14.1	−97.5
La Madera pool (a)	1.67	0.30	0.29	0.49	BDL	367	−14.4	−100.1
La Madera pool (a)	0.93	0.41	0.24	0.60	BDL	269	−14.2	−99.2
Ojo Caliente Well (a)	15.4	0.69	4.29	1.42	0.21	351	−14.5	−107.5
Ojo Caliente Lithium spring (a)	13.1	0.66	4.20	1.34	0.19	352	−14.7	−107.3
Ojo Caliente Iron spring (a)	14.1	0.78	4.26	1.43	0.20	307	−14.4	−106.7
Statue spring (a)	1.54	0.29	0.51	0.52	0.04	434	−13.8	−99.1
Statue spring (a)	0.87	0.52	0.21	0.53	BDL	189	−14.0	−98.3
Eastern Rio Grande rift springs								
Black Rock spring (a)	3.0	0.59	0.42	0.30	0.04	115	−14.7	−103.3
Manby spring (a)	3.5	1.18	0.27	0.29	0.02	43.3	−14.4	−103.9
Bear Crossing spring (a)	0.88	0.55	0.03	0.07	0.01	14.1	−15.4	−105.7
Ponce de Leon spring (a)	12.7	0.74	0.37	0.57	0.01	150	−13.2	−94.4
Meteoric Waters in study area								
Big spring (a)	1.1	BDL	0.13	0.07	0.03	NR	−15.1	−106.8
Taos Junction spring (a)	1.7	BDL	0.18	0.17	0.02	NR	−15.3	−108.4
Rio Grande Spring (a)	0.95	0.09	0.16	0.08	0.02	51.4	−14.7	−102.9
No Agua well (a)	0.37	0.45	0.01	0.03	BDL	5.5	−14.8	−105.3
Tusas warm Spring (a)	0.18	BDL	BDL	0.03	BDL	NR	−15.8	−109.5
Picuris warm Spring (a)	0.15	BDL	0.03	0.03	0.03	NR	−13.8	−95.5
Valles Caldera springs and wells								
Footbath (b)	10.6	<0.4	0.17	0.2	NR	NR	−20.4	−82.1
Women bath (b)	5.2	<0.4	0.17	0.2	0.04	NR	−8.5	−60.8
Valles Caldera well VC-2A (b)	5.7	5.9	26.5	25.6	1.92	499	−7.1	−74.4
Valles Caldera well VC-2B (b)	5.7	13.6	32.8	29.6	<0.1	305	−7.5	−85.2
Baca well 13 (b)	7.2	5.3	17.0	17.0	1.6	358	−9.9	−87.0
Baca well 15 (b)	5.5	5.9	15.0	17.0	2.3	355	−8.5	−84.0
Baca well 24 (c)	NR	NR	NR	NR	NR	NR	−8.6	−82.0
Baca well 4 (c)	NR	NR	NR	NR	NR	NR	−10.0	−87.5
Valles Caldera SW geothermal outflow springs								
Soda Dam (b)	3.3	4.6	13.8	12.1	1.5	329	−10.6	−84.9
Jemez spring (b)	5.0	2.4	8.9	7.34	0.7	377	−10.5	−81.9

(a) This study; (b) Goff and Gardner, 1994; (c) Truesdell and Janik, 1986.
NR - Not Reported.
BDL - Below Detection Limit.

3.3. Sources of CO_2 - Carbon isotope calculations

Quantifying the amount of carbon from different reservoirs using water chemistry was developed by Fontes and Garnier (1979), further explained in Chiodini et al. (2004), and modified in Crossey et al. (2009). The three sources of carbon are from the dissolution of carbonates (C_{carb}), organic sources such as soil and plant degassing (C_{org}), and endogenic sources such as magmas and CO_2 from geothermal fluids (C_{endo}). These sources of carbon contribute to the total DIC (H_2CO_3, HCO_3, CO_3).

To correct for any Ca^{2+} and Mg^{2+} derived from gypsum and other sulfates, SO_4^{2-} activity was subtracted from the concentration of Ca^{2+} and Mg^{2+} (in mol/L). Then C_{carb} was calculated by adding the concentrations (in mol/L) of remaining Ca^{2+} and Mg^{2+} as the molar equivalent of CO_2 dissolved from limestone and dolomite. This results in a minimum estimation of the carbon derived from dissolution of carbonates and sulfates, termed C_{carb}. The C_{carb} calculation is shown in the following mass balance: $C_{carb} = Ca^{2+} + Mg^{2+} - SO_4^{2-}$. C_{carb} is then subtracted from the total DIC to derive external carbon (C_{ext} = DIC – C_{carb}). C_{ext} is then resolved into model endmembers C_{org} and C_{endo} using stable isotopes. This involves adjusting the measured carbon isotope value to "remove" the proportion due to C_{carb} which is assigned a value of $\delta^{13}C$-$CaCO_3$ = 0 to 1‰ typical of sedimentary inorganic carbon (carbonates) (Sharp, 2007). This study used 0‰ because the Pennsylvanian Madera Limestone is common in northern New Mexico (Crossey et al., 2011).

This correction results in the carbon isotope value of the external carbon shown in the equation below:

$$\delta^{13}C_{ext} = \left(\left(\delta^{13}C_{DIC} * DIC\right) - \left(\delta^{13}C_{carb} * C_{carb}\right)\right)/C_{ext} \text{(Crossey et al., 2009)} \quad (3)$$

4. Results

The western springs were more acidic and had higher conductivity measurements than the eastern springs (Table 1). The pH at Ojo Caliente was 6.63, La Madera was 6.02, and Statue spring was 6.34. Conductivity at Ojo Caliente was 4240 μS, La Madera was 1250 μS, and Statue spring was 1610 μS. The highest temperature at Ojo Caliente was 53.2 °C, La Madera was 26.1 °C, and Statue spring was 28.5 °C. Springs on the eastern side of the RGR had a pH range of 7.0 to 8.6, conductivity ranged from 232 to 830 μS, and temperature ranged from 16.8 to 39.1 °C.

Fig. 4 shows the stable isotope data of oxygen and hydrogen (Table 2). Springs from both the western and the eastern sides of the RGR plot to the left of the GMWL with the exception of the Ojo Caliente springs, which plot on and to the right of the GMWL. Four groups of meteoric waters (blue symbols) were plotted on Fig. 4. Three of the meteoric groups plot to the left of the GMWL, including rivers in the Sangre de Cristo Mountains (Tolley, 2014), springs of the Taos Plateau (this study), and groundwater samples from the Taos Plateau (Johnson and Bauer, 2012). The Johnson and Bauer (2012) groundwater data was used to create the Taos Plateau Local Meteoric Water Line. The fourth meteoric group was the groundwater samples near the town of Taos (Drakos et al., 2004), which plot to the right of the GMWL. Well water samples from the Valles Caldera and the southwestern outflow springs of the Valles Caldera (Soda Dam and Jemez springs) plot along a subhorizontal trend to the right of the GMWL (Goff and Gardner, 1994).

In Fig. 5, meteoric springs of the Taos Plateau plot near the Ca^{2+}–HCO_3^- corner of the parallelogram of the Piper diagram. Of the western springs, Ojo Caliente springs had dominantly Na^+–HCO_3^- ions and La Madera/Statue springs were characterized by Ca^{2+}-Na^+-SO_4^{2-}–HCO_3^- ions (Table 3A). Ojo Caliente springs had particularly high [Na^+] and [HCO_3^-] compared to La Madera/Statue springs. Ojo Caliente springs had [Na^+] of 983 mg/L whereas La Madera/Statue springs had [Na^+] of 160 to 193 mg/L; and Ojo Caliente springs had [HCO_3^-] of 2027 mg/L whereas La Madera/Statue springs had [HCO_3^-] of 660 to 790 mg/L. The eastern springs plot along a mixing trend on the Piper parallelogram from Ca^{2+}–HCO_3^- to Na^+-Cl^- waters. The eastern springs had the lowest [HCO_3^-] of 92 to 204 mg/L. The Valles Caldera springs (WOM and FB) were acid sulfate waters, therefore they plot near the SO_4^{2-} corner of the anion triangle of the Piper diagram. The Valles Caldera wells (VC and Baca wells) plot near the Cl^- corner of the anion triangle and in the Na^+-Cl^- corner of the parallelogram (Goff and Gardner, 1994).

Ojo Caliente springs had greater concentrations of trace elements than the eastern and other western springs of this study (Table 2). Ojo Caliente results were [Li] at 4.29 mg/L and [B] at 1.43 mg/L. The La Madera/Statue springs, on the western side, had lower [Li] at 0.29 mg/L and [B] at 0.54 mg/L and the eastern RGR springs also had lower [Li] at

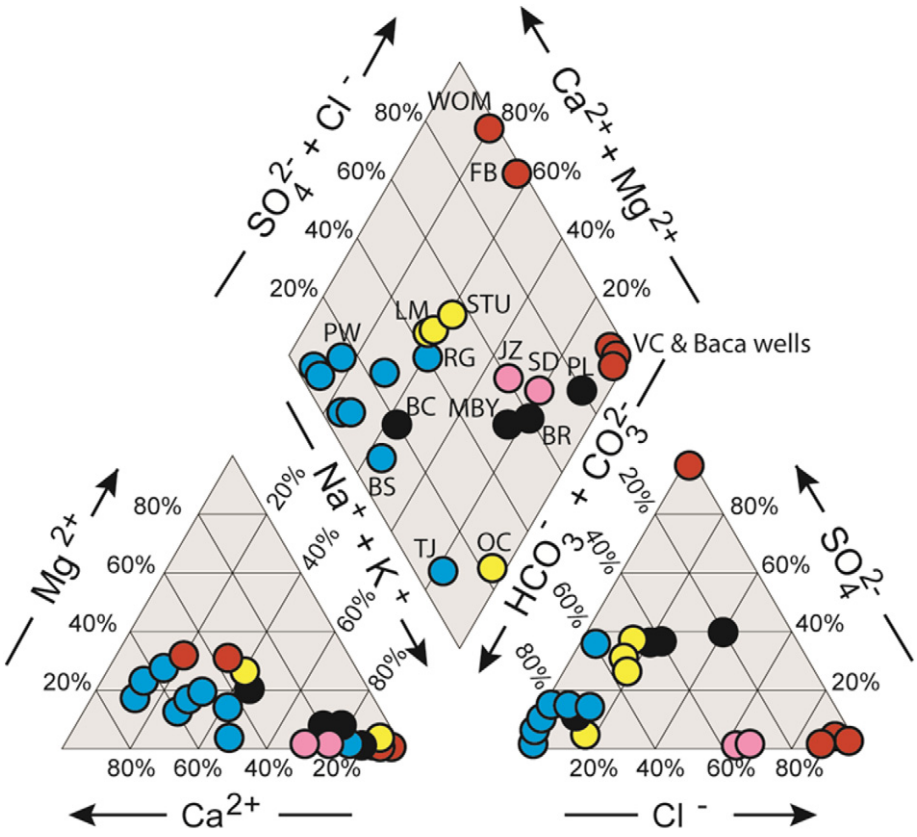

Fig. 5. Piper diagram of the study area and Valles Caldera water samples. The Piper diagram relates water samples based on major ions. The blue symbols are more meteoric and generally plot in the left-hand corner (Ca^{2+}–$HCO3^-$) of the parallelogram. The yellow symbols represent spring water from the western RGR, which have a large range of water types. The black symbols represent spring water from the eastern RGR and show a mixing trend from Ca^{2+}–$HCO3^-$ to Na^+-Cl^- waters. The geothermal plume waters of the Valles Caldera, represented by pink symbols, plot near the Na^+-Cl^- corner.

Table 3
Major ion concentrations (mg/L).

Sample name	Ca	Mg	Na	K	HCO_3	Cl	SO_4	Balance %
Western Rio Grande rift springs								
La Madera Mother spring (a)	138	52.5	174	18.2	674	101	268	−0.5
La Madera pool (a)	148	55.2	185	20.7	790	109	286	−3.4
Ojo Caliente Well (a)	19.5	6.5	980	34.5	2027	243	150	2.1
Ojo Caliente Lithium spring (a)	24.1	9.2	949	32.2	2011	232	146	1.7
Ojo Caliente Iron spring (a)	21.9	7.9	983	33.3	2026	239	148	2.6
Statue spring (a)	129	56.3	160	13.3	660	128	216	−1.6
Statue spring (a)	133	50.2	160	17.9	703	97.9	252	−3.6
Eastern Rio Grande rift springs								
Black Rock spring (a)	21.2	5.2	149	11.7	196	68.0	141	1.1
Manby spring (a)	24.6	4.7	128	9.8	204	51.1	131	−0.6
Bear Crossing spring (a)	16.3	4.9	20.5	2.8	110	7.7	11.5	−1.6
Ponce de Leon spring (a)	10.7	0.7	150	4.1	91.5	111	150	−3.6
Meteoric Waters in study area								
Big spring (a)	29.5	1.7	28.3	4.9	164	2.2	10.8	−0.1
Taos Junction spring (a)	14.4	1.5	101	4.1	282	2.8	20.8	1.9
Rio Grande Spring (a)	34.4	6.2	33.2	3.4	141	4.8	68.0	−1.4
No Agua well (a)	23.9	4.9	10.4	4.6	115	2.5	3.2	3.2
Tusas warm Spring (a)	30.8	4.2	4.3	2.1	137	0.9	1.3	−4.0
Picuris warm Spring (a)	5.3	1.4	1.3	0.8	20.7	0.6	2.5	0.8
Valles Caldera springs and wells								
Footbath (b)	56	26.5	10.8	94	BDL	BDL	7900	−81
Women bath (b)	131	50	18.9	72	BDL	1.5	6400	−90
Valles Caldera well VC-2A (b)	5.9	0.14	1842	308	273	2943	55	−0.2
Valles Caldera well VC-2B (b)	78.5	0.76	2350	700	105	4150	7.8	2.1
Baca well 13 (b)	3.4	0.04	1146	244	168	1897	42	−0.8
Baca well 15 (b)	12.4	0.02	1196	261	48	2093	29	−0.9
Valles Caldera SW geothermal outflow springs								
Soda Dam (b)	331	23.6	1006	180	1527	1513	35.3	−1.2
Jemez spring (b)	129	4.7	644	69.0	729	905	41.5	−2.3
Zia hot well (b)	282	54.8	3320	63.3	1445	2890	3030	−1.1

(a) this study; (b) Goff and Gardner, 1994.
BDL - below detection limit.

0.42 mg/L and [B] at 0.57 mg/L. Ojo Caliente had the greatest Cl/Br ratio of 433, La Madera had the next greatest at 244, and the eastern springs ranged from 14 to 150 (Table 2).

Fig. 6 is a plot of the total carbon concentrations derived from external sources (C_{ext} in mol/L) versus the external carbon isotope value ($\delta^{13}C_{ext}$ in ‰). Samples plot on mixing arrays using idealized end members (Craig, 1953). The organic $\delta^{13}C$ endmember range is −22 to −34‰ for C3 plants, −9 to −16‰ for C4 plants (Robinson and Scrimgeour, 1995), and − 15 to −19‰ for arid soils from west Texas (Deines et al., 1974). The C_{endo} $\delta^{13}C$ endmember was derived empirically from Ojo Caliente (this study) and Valles Caldera data (Goff and Gardner, 1994; Goff and Janik, 2002), which ranged from −2.5 to −6.8‰. Valles Caldera values were corrected for C_{carb} using the same method as springs in this study. The range of Ojo Caliente $\delta^{13}C$ values was likely affected by sampling technique, as noted by the samples collected in copper tubes at various locations had more depleted values than those collected in HDPE bottles. We theorize that the samples collected in the HDPE containers degassed as the bottle was opened causing increased ratios. As a result of degassing, the upper $\delta^{13}C$ end member of Ojo Caliente values may be artificially high.

As a reference for endogenic carbon isotopes values, northern New Mexico and Colorado ranged from −3 to −5‰ (Crossey et al., 2011; Karlstrom et al., 2013). Similar ranges were measured in the axial rift zones of Iceland of −3.7 to −5.3‰ (Barry et al., 2014), the Icelandic plume of −3.8‰ (Poreda et al., 1992), the Galapogos Archipelago of −3.5‰ (Goff et al., 2000), and the Kilauea Volcano in Hawaii of −4.1 to −3.4‰ (Gerlach and Taylor, 1990). These values are in range of mantle values of −6.5 ± 2.5‰ (Sano and Marty, 1995). The inset triangular plot in Fig. 6 shows the resulting proportions of the carbon sources based on carbon isotopes using the calculation in Section 4 "Sources of CO_2 – Carbon isotope calculation."

In Fig. 6, the Valles Caldera geothermal outflow plume waters (pink symbols) plot along the same mixing line defined by Ojo Caliente and Valles Caldera values. La Madera springs also plot along this mixing line with a C_{ext} concentration of 0.026 mol/L and $\delta^{13}C_{ext}$ of −2.4‰. The eastern springs, Manby and Black Rock, had $\delta^{13}C_{ext}$ values similar to the western springs of −3.6 and − 4.5‰, though they had lower C_{ext} concentrations of 0.0038 and 0.0030 mol/L. The two other eastern springs, Bear Crossing and Ponce de Leon, had $\delta^{13}C$ values of −7.2 and − 9.2‰, which plot closer to an organic source. Carbon isotope data is shown in Table 4.

Strontium results showed a large variation among spring locations. Ojo Caliente springs had $^{87}Sr/^{86}Sr$ ratios of 0.747 and [Sr] of 1.35 mg/L, La Madera and Statue springs had lower $^{87}Sr/^{86}Sr$ ratios of 0.718 and [Sr] of 1.07 to 1.15 mg/L (Table 5). Spring waters on the eastern side of the RGR had the lowest $^{87}Sr/^{86}Sr$ ratios ranging from 0.708 to 0.713 and [Sr] of 0.39 to 0.42 mg/L. The eastern spring group values were similar to the Rio Grande River values in northern New Mexico (Mills, 2003) (Fig. 7). The Valles Caldera VC-wells had similar [Sr] as Ojo Caliente and La Madera/Statue springs of 0.76 to 1.22 mg/L, and a similar range of $^{87}Sr/^{86}Sr$ ratios of 0.71867 to 0.73690 (Goff and Gardner, 1994). The Valles Caldera Women's bathhouse spring (WOM) had low [Sr] because the spring water mostly formed from vapor that condensed to a liquid. Dissolved strontium is not volatile, therefore fluids formed from condensed gases would not contain strontium.

The abundances of Ar-N_2-He in Fig. 8 show differences among the sides of the RGR. The western springs plot along a mixing line between helium-rich gases and air. Conversely, the eastern springs do not plot along this mixing line, because they had excess N_2 (Table 6). The second difference between the sides of the RGR was higher CH_4 abundance in the western springs. Ojo Caliente had CH_4 gas abundances of 0.02 to 0.09% and La Madera/Statue springs had 0.01 to 0.26%, whereas all of the eastern springs had non-detectable CH_4 with the exception of Manby at 0.01%.

In Fig. 9, R_C/R_A values are presented along the bottom axis of the trilinear plot of ^3He, ^4He and CO_2. Helium isotope values in the western springs were 0.14 to 0.39 R_C/R_A and eastern spring values were 0.13 to 0.32 R_C/R_A (Table 7), therefore among both east and west sides of the RGR there is 1.6 to 4.8% mantle derived helium assuming a MORB end member of 8 ± 1 R_A (Craig and Lupton, 1976; Craig, 1977; Poreda et al., 1992). Valles Caldera data (Goff and Janik, 2002) plot closer to the ^3He apex and spread along the $CO_2/^3He$ axis. The $CO_2/^3He$ values at Ojo Caliente and La Madera/Statue springs ranged from 9.92×10^9 to 1.14×10^{10} and 8.91×10^{10} to 4.56×10^{11}, respectively, and the eastern springs ranged from 1.60×10^{10} to 4.03×10^{10}.

The western springs had higher P_{CO2} and CO_2 concentrations than the eastern springs. The modeled P_{CO2} of the western springs ranged from $10^{-0.33}$ to $10^{0.04}$ atm (Table 8); CO_2 gas contents ranged from 0.03 to 30.7% from samples in collected in Giggenbach bottles and vials (Table 6) and 41 to 86% (measured as ccSTP/cc) from samples collected in copper tubes (Table 7). The eastern springs had P_{CO2} values closer to atmospheric values ($10^{-3.5}$) (Drever, 1997) ranging from $10^{-1.62}$ to $10^{-3.64}$; CO_2 gas content ranged from 0.02 to 4.27% from samples collected in Giggenbach bottles and 32 and 33% from samples collected in copper tubes. Similarly, the pH measurements of the western springs are more acidic than the eastern springs. The pH range of the western springs was 5.77 to 6.68 and the eastern springs was 7.0 to 8.60.

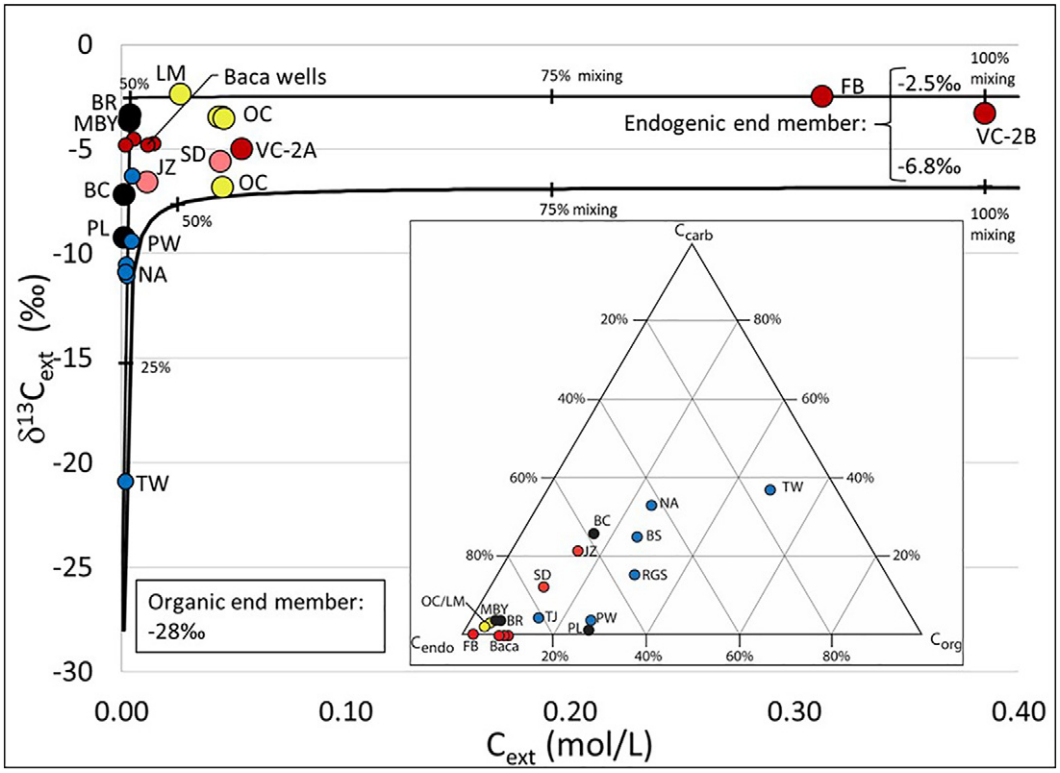

Fig. 6. External carbon plot of $\delta^{13}C_{ext}$ vs. C_{ext} concentration. The carbon load in springs is modeled as three components: CO_2 derived from dissolved carbonates, soil degassing from organic material, and CO_2 derived from endogenic degassing. The curved line is a mixing line between organic and endogenic carbon, and these end members added together is external carbon (C_{ext}). The organic end member has low external carbon concentrations and more negative $\delta^{13}C_{ext}$ values; the endogenic end member has high external carbon concentrations and $\delta^{13}C_{ext}$ values empirically bracketed at −2.5 to −6.8‰. The bracketed endogenic values are established by Valles Caldera waters shown as red symbols (Goff and Janik, 2002; Truesdell and Janik, 1986) and Ojo Caliente springs shown as yellow symbols with $\delta^{13}C_{ext}$ of −3.5 to −6.8‰. Of the springs in the study area, the western springs (yellow symbols) had greater external carbon concentrations than the eastern springs (black symbols) as shown along the x-axis. Among the eastern springs, Manby and Black Rock had $\delta^{13}C_{ext}$ values characteristic of endogenic origins (−3.6 and − 4.5‰), and Bear Crossing and Ponce de Leon had lighter $\delta^{13}C_{ext}$ values (−7.2 and − 9.2‰) trending towards the organic end member. The inset is a trilinear diagram showing the percentages of each CO_2 source. Most of the springs in the study plot near the endogenic apex and the meteoric springs (blue symbols) trend away from the endogenic apex and have about equal percentages of C_{carb} and C_{org}.

5. Discussion

Goff and Gardner (1994) studied the hydrochemistry of the Valles Caldera geothermal waters and showed a geothermal outflow plume flowing along the Jemez fault and discharging at springs, in particular at Soda Dam and Jemez springs. McGibbon et al. (2018) extended this idea by studying spring waters further southwest along the Jemez fault near San Ysidro, NM. Evidence of distal effects of the Valles Caldera in San Ysidro springs are shown with carbon isotopes, CO_2 abundance, non-reactive gases, and presence of travertine deposits (McGibbon et al., 2018). Gas data from the Valles Caldera, Soda Dam, Jemez, and San Ysidro springs (Goff and Janik, 2002; McGibbon et al., 2018) plotted against distance from the Valles Caldera reveal exponential trends exposing possible distal effects of the Valles Caldera at distances of 50 km, which is further than previously accepted (Figs. 10 & 11). The exponential trend may be related to the gas-phase migrating and partitioning lighter gases during transport (Darrah et al., 2013).

With the same type of data plotted to the northeast of the Valles Caldera, exponential chemical trends are not as apparent, though this could be due to lack of data at closer distances to the Valles Caldera. Additional springs to the northeast are plotted to show regional trends, including Chimayó and Abiquiú. Even though these trends to the northeast are not as well defined, distal influences of the Valles Caldera to the northeast may become apparent by comparing the hydrochemistry of the east and west sides of the RGR in northern New Mexico with that of the Valles geothermal system.

5.1. Discussion: comparison of eastern and western spring groups

The eastern (BR, MBY) and western (OC, LM, STU) spring groups of the RGR share two commonalities: 1) the isotopes of hydrogen and oxygen showed that waters are dominantly of meteoric origin, and 2) detectable amounts of mantle gases were present according to their helium isotopic ratios. Many differences in hydrochemistry were apparent on either side of the RGR and is discussed in the following paragraphs.

Analytical data showed Cl^- as the dominate anion in the eastern springs and HCO_3^- in the western springs (Fig. 5). Among the western springs, La Madera/Statue springs had a larger proportion of SO_4^{2-} than Ojo Caliente springs. The differences in major ions among Ojo Caliente and La Madera/Statue springs could be from different water-rock reactions, for example La Madera/Statue could have equilibrated with gypsum increasing SO_4^{-2}. The most notable difference among all the springs in terms of major ion chemistry was greater $[Na^+]$ and $[HCO_3^-]$ in Ojo Caliente springs.

Ojo Caliente springs contained higher concentrations of geothermally-related trace elements (Figs. 12A–B) and Cl/Br ratios compared to both the La Madera/Statue and the eastern springs. Low Cl/Br ratios reveal meteoric origins and high ratios are indicative of saline subsurface waters (Phillips et al., 2003; Hogan et al., 2007). The differences among the western springs, La Madera/Statue and Ojo Caliente, may be due to different water rock interactions, or La Madera/Statue springs could have mixed with a greater volume of a shallow/meteoric water.

Table 4
Carbon isotope and DIC.

Sample name	Sample Container	Measured $\delta^{13}C$ (‰)	$\delta^{13}C_{ext}$ (‰)	DIC (mol/L)	C_{carb} (mol/L)	C_{ext} (mol/L)	C_{carb}(%)	C_{org} (%)	C_{endo} (%)
Western Rio Grande rift springs									
La Madera Mother (a)	HDPE	−1.02	−1.1	0.0285	0.0028	0.026	8.0	0	92.0
La Madera Mother (a)	CT	−2.20	−2.4	0.0285	0.0023	0.026	8.0	0	92.0
La Madera pool (a)	HDPE	2.32	2.8	0.0212	0.0034	0.018	16.1	0	83.9
La Madera pool (a)	HDPE	3.47	3.8	0.0332	0.0030	0.030	9.0	0	91.0
Ojo Caliente Well (a)	HDPE	−3.47	−3.5	0.0454	0.0003	0.046	0.6	3.9	95.5
Ojo Caliente Well (a)	CT	−6.80	−6.8	0.0454	0.0003	0.045	0.6	16.8	82.6
Ojo Caliente Lithium spring (a)	HDPE	−3.45	−3.5	0.0440	0.0004	0.045	0.9	3.5	95.6
Ojo Caliente Iron spring (a)	HDPE	−3.54	−3.6	0.0460	0.0003	0.047	0.7	4.3	95.0
Statue spring (a)	HDPE	0.36	0.4	0.0201	0.0033	0.017	16.3	0	83.7
Eastern Rio Grande rift springs									
Black Rock spring (a)	HDPE	−4.23	−4.5	0.0032	0.00018	0.0030	5.7	7.4	87.0
Manby spring (a)	HDPE	−3.47	−3.6	0.0039	0.00020	0.0038	4.9	4.1	91.0
Bear Crossing spring (a)	HDPE	−5.32	−7.2	0.0019	0.00049	0.0014	26.0	13.6	60.3
Ponce de Leon spring (a)	HDPE	−9.05	−9.2	0.0015	0.00003	0.0014	2.0	25.7	72.2
Meteoric Waters in study area									
Big spring (a)	HDPE	−7.90	−10.5	0.0028	0.00069	0.0021	25.0	23.5	51.5
Taos Junction spring (a)	HDPE	−6.00	−6.3	0.0047	0.00020	0.0045	4.3	14.3	81.4
Rio Grande Spring (a)	HDPE	−9.33	−11.0	0.0026	0.00040	0.0022	15.6	28.1	56.3
No Agua well (a)	HDPE	−7.25	−10.9	0.0023	0.00076	0.0015	33.3	22.0	44.7
Tusas warm Spring (a)	HDPE	−13.11	−20.9	0.0025	0.00093	0.0016	37.1	45.4	17.5
Picuris warm Spring (a)	HDPE	−9.04	−9.4	0.0045	0.00017	0.0043	3.7	26.0	70.2
Valles Caldera springs and wells									
Footbath (b)	Gas sampling bottle	−2.47	−2.5	0.314	0.0011	0.31	0.4	0	99.6
Valles Caldera well VC-2A (b)	Gas sampling bottle	−4.99	−5.0	0.054	BDL	0.054	0	9.8	90.2
Valles Caldera well VC-2B (b)	Gas sampling bottle	−3.30	−3.3	0.387	0.0019	0.385	0.5	3.2	96.3
Baca well 13 (c)	Gas sampling bottle	−4.51	−4.5	0.0053	BDL	0.0053	0	7.9	92.1
Baca well 15 (c)	Gas sampling bottle	−4.77	−4.8	0.0015	BDL	0.0015	0	9.0	91.0
Baca well 24 (c)	Gas sampling bottle	−4.80	−4.8	0.012	BDL	0.012	0	9.0	91.0
Baca well 4 (c)	Gas sampling bottle	−4.73	−4.7	0.014	BDL	0.014	0	8.7	91.3
Valles Caldera SW geothermal outflow springs									
Soda Dam (b)	Gas sampling bottle	−4.90	−5.6	0.050	0.0062	0.044	12.3	10.7	77.1
Jemez spring (b)	Gas sampling bottle	−5.15	−6.6	0.015	0.0032	0.011	21.9	12.6	65.5

(a) This study; (b) Goff and Janik, 2002; (c) Truesdell and Janik, 1986.
Valles Caldera and geothermal outflow plume samples were dry gas.
HDPE - Carbon isotopes analyzed from water collected in a high density polyethylene bottle.
CT - Carbon isotopes analyzed from gases exolved from water in a copper tube.
BDL - Below detection level.

The highest $^{87}Sr/^{86}Sr$ ratios were observed from Ojo Caliente springs (Fig. 7) and is interpreted as long fluid flow through granitic bedrock. Lower $^{87}Sr/^{86}Sr$ ratios were measured at La Madera/Statue springs compared to Ojo Caliente, which could again be due to different water-rock interactions or greater contribution of a shallow mixing end member in La Madera/Statue springs. The eastern spring $^{87}Sr/^{86}Sr$ ratios were slightly lower than La Madera/Statue springs.

The fourth major contrast is greater [He] measured in Ojo Caliente springs. In Fig. 8, Ojo Caliente and La Madera/Statue springs form a mixing line from He-rich samples to excess air-saturated samples (Weiss, 1971a, 1971b). Ojo Caliente springs plot near the He apex and La Madera/Statue springs plot as gases enriched in N_2/Ar, related to either the introduction of excess N_2 or N_2/Ar fractionation during fluid transport (Snyder et al., 2003; Darrah et al., 2013). Based on the lack of excess air components (e.g., extreme Ar or Kr enrichment) in most samples and low Kr/Ar (Table 7), we suggest that although the trend appears to be a mixture between a helium-rich end-member and air, it actually relates to mixing between a helium-rich end-member and a migrated gas-phase that has partitioned lighter gases (Ne, N_2) preferentially into the gas phase and/or accumulated excess N_2 during transport (Darrah et al., 2013). The partitioning of lighter gases occurs by a carrier gas, typically CO_2, percolating through water and extracting dissolved gasses such as Ne or N_2; accumulated excess N_2 during transport occurs by water-rock interaction of mantle derived fluids with shallow crust (Darrah et al., 2013). The eastern springs show unclear mixing trends in Fig. 8, but all have a greater abundance of N_2 than the western springs, showing the spring groups are unrelated. Excess N_2 found in the eastern springs is consistent with the interactions between geothermal fluids and clay minerals rich in organic matter and organic nitrogen.

The defining feature of the western springs are higher abundances of CH_4, CO_2, C_{endo} (deep carbon), HCO_3, and P_{CO2} than the eastern springs. The eastern springs had no detectable CH_4 with the exception of Manby spring at a low concentration. CH_4 in the western springs is not believed to be associated with hydrocarbons due to no evidence of longer hydrocarbon chains, and is instead associated with reactions within hydrothermal systems among CO_2 and H_2 (Welhan, 1988). This abiotic CH_4 coupled with greater abundances of CO_2, C_{endo}, HCO_3, and higher P_{CO2} suggest the western springs are more carbonic. Higher P_{CO2} values likely affected pH values since the western springs were more acidic than the eastern springs.

Springs on both sides of the RGR had similar $\delta^{13}C_{ext}$ values and were all within range of endogenic carbon (only considering Black Rock and Manby on the eastern side). Our interpretation is that these springs have deeply derived CO_2 based on carbon isotopes, but the eastern springs have both lower fluxes of mantle-derived CO_2 and a higher proportion of CO_2 derived from the breakdown of organic matter and

Table 5
Radiogenic strontium ratios and concentrations.

Sample name	Sample date	Latitude	Longitude	$^{87}Sr/^{86}Sr$	Sr (mg/L)	Rb (mg/L)	Host rock/aquifer
Western Rio Grande rift springs							
La Madera Mother Spring (a)	1/4/2015	36.361000	−106.041930	0.718301	1.15	NA	Quaternary travertine
Ojo Caliente Well (a)	9/10/2015	36.305492	−106.051980	0.747376	1.30	NA	Precambrian metarhyolite
Ojo Caliente Iron Spring (a)	9/10/2015	36.304346	−106.053002	0.746596	1.35	NA	Precambrian metarhyolite
Statue Spring (a)	9/10/2015	36.382080	−106.060130	0.718129	1.07	NA	Santa Fe Group
Eastern Rio Grande rift springs							
Black Rock Spring (a)	1/6/2015	36.530668	−105.712160	0.707885	0.41	NA	Tertiary Servilleta basalt
Manby Spring (a)	9/10/2015	36.5083	−105.7241	0.707994	0.39	NA	Tertiary Servilleta basalt
Ponce de Leon Spring (a)	1/6/2015	36.323830	−105.506200	0.713287	0.23	NA	Ojo Caliente SS and Servillta Basalt
Meteoric Waters in study area							
Taos Junction Spring (a)	1/5/2015	36.334180	−105.736540	0.707761	0.27	NA	Santa Fe Group
Rio Grande river samples							
Taos Junction Campground (b)	January 2001	36.336147	105.733700	0.708936	0.36	NA	River Sample
Cochiti Dam (b)	August 2001	35.616908	106.325053	0.709607	0.55	NA	River Sample
Cochiti Dam (b)	January 2001	35.616908	106.325053	0.709745	0.64	NA	River Sample
Albuquerque (b)	August 2001	35.089320[a]	−106.680502[a]	0.709672	0.77	NA	River Sample
Albuquerque (b)	January 2001	35.089320[a]	−106.680502[a]	0.709931	0.84	NA	River Sample
Valles Caldera springs and wells							
Jemez Women bathroom (c)	June 1985	35.906420	−106.616397	0.710614	0.14	0.1	Bandelier tuff and Rhyolite
VC-2A (d)	8/27/1987	35.907595	−106.615534	0.718670	0.76	4.3	Hydrothermally altered zone
VC-2B (d)	1/17/1990	35.91013	−106.60949	0.736900	1.22	11.5	Hydrothermally altered zone
Baca 13 well in Redondo Graben (c)	1982–1988	35.896512	−106.568831	0.708423	0.14	2.7	Lower Bandelier tuff and andesites (Keres group)
Baca 15 (c)	Sept. 1982	35.893188	−106.580717	0.709412	0.13	3.1	Lower Bandelier tuff and andesites (Keres group)
Valles Caldera SW geothermal outflow springs							
Soda Dam (c)	June 1985	35.792289	−106.686790	0.721932	1.5	1.8	Altered limestone, Madera and Sandia Formation
Jemez spring (c)	June 1985	35.772038	−106.690775	0.721742	0.61	0.7	Altered limestone and shale, Madera Formation
Zia hot well in SE SJ Basin (c)	June 1985	35.64559	−106.88910	0.715564	7.74	0.2	Paleozoic and Mesozoic sedimentary rocks
Valles Caldera rocks							
VC-1 core hole (c)	Sept. 1985	35.85	−106.61	0.715220	1.16	0.4	Altered limestone, Madera Formation
VC-1 core hole (c)	May 1986	35.85	−106.61	0.715398	0.76	0.35	Altered limestone, Madera Formation
VC-1 (d)	9/5/1985	35.85	−106.61	0.715220	1.33	0.4	NR
VC-1 (c)	Summer 1984	35.85	−106.61	0.704854	<300	137	Upper VC-1 tuff, whole rock
VC-1 (c)	Summer 1984	35.85	−106.61	0.704766	<300	137	Middle VC-1 tuff, whole rock
VC-1 (c)	Summer 1984	35.85	−106.61	0.704593	aprox. 750	aprox. 60	Andesiteic volcanic breccia
VC-1 (c)	Summer 1984	35.85	−106.61	0.709709	aprox. 30	aprox. 165	Rhyolite in volcanic breccia
VC-1 (c)	Summer 1984	35.85	−106.61	0.721411	NR	NR	Shale, La Madera Limestone
VC-1 (c)	Summer 1984	35.85	−106.61	0.716129	NR	NR	Altered limestone, in La Madera Limestone
VC-1 (c)	Summer 1984	35.85	−106.61	0.716355	NR	NR	Calcite vein, La Madera Limestone
VC-1 (c)	Summer 1984	35.85	−106.61	0.756860	NR	NR	Shale, Sandia Formation
VC-1 (c)	Summer 1984	35.85	−106.61	0.726106	NR	NR	Altered limestone breccia, Sandia formation
Wells in Taos							
BOR 2A (e)	5/8/2002	36.382496	−105.599314	0.7123	NR	NR	Quaternary
Yaravitz (e)	5/7/2002	36.529307	−105.560466	0.7100	NR	NR	Precambrian
OW6 (e)	5/9/2002	36.442708	−105.562476	0.7113	NR	NR	Agua Azul (Servilleta Formation)
Landfill MW-1 (e)	5/9/2002	36.449635	−105.638763	0.7094	NR	NR	Agua Azul (Servilleta Formation)
BOR2B (e)	5/8/2002	36.382604	−105.599393	0.7156	NR	NR	Tertiary
RP2500 (e)	5/1/2002	36.377900	−105.663773	0.7086	NR	NR	Tertiary
BOR1-Deep (e)	5/9/2002	36.346765	−105.644987	0.7106	NR	NR	Tertiary
BOR 7 (e)	6/13/2002	36.494068	−105.622135	0.7074	NR	NR	Tertiary
BIA 9 (e)	6/13/2002	36.494068	−105.622135	0.7095	NR	NR	Quaternary
BOR 5 (e)	8/1/2002	36.466981	−105.5877085	0.7093	NR	NR	Quaternary

(a) This study; (b) Mills, 2003; (c) Vuataz et al., 1988; (d) Goff and Gardner, 1994; (e) Drakos et al., 2004.
NA - Not Analyzed.
NR - Not Reported.
[a] Coordinates estimated from Google Earth.

crustal carbonates. The presence of carbonic springs only on the western side is an important finding because it raises the question of CO_2 origins.

In summary, within the study area, Ojo Caliente waters had the highest concentrations of Na, Cl, Li, B, HCO_3, C_{endo}, Sr, He, highest $^{87}Sr/^{86}Sr$ ratios, and $\delta^{13}C_{ext}$ values typical of endogenic carbon. La Madera/Statue springs had lower amounts endogenic tracers compared to Ojo Caliente. The eastern springs had the lowest presence of endogenic tracers and excess N_2 (non-air-derived). Differences in water chemistry among Ojo Caliente and La Madera/Statue springs is interpreted as different water rock interaction and/or greater contribution of shallow/meteoric input into La Madera/Statue springs. The main similarity among Ojo Caliente and La Madera/Statue springs is the carbonic nature of the springs shown with higher concentrations of CH_4, C_{endo}, CO_2, HCO_3, and P_{CO2}.

5.2. Discussion: comparison of Valles Caldera to Ojo Caliente

To explain greater concentrations of endogenic components in Ojo Caliente springs, the Valles Caldera spring and well chemistries were

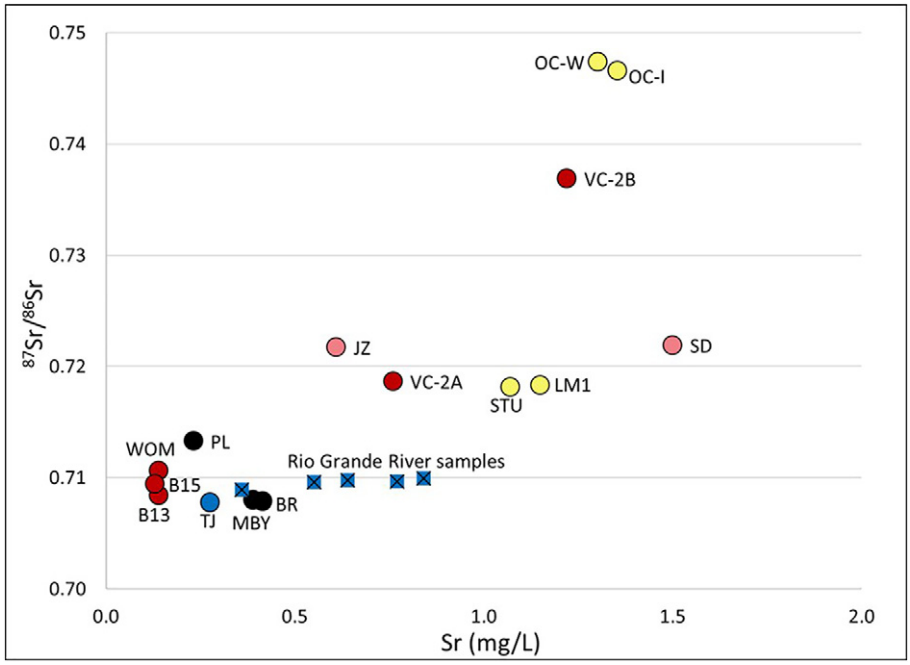

Fig. 7. Strontium isotope ratios versus strontium concentration. Both parameters were the greatest at Ojo Caliente compared to the remainder of the springs in the study area. Higher radiogenic strontium in Ojo Caliente spring waters is evidence of water flowing through Precambrian granitic bedrock. The Valles Caldera VC-wells (Goff and Janik, 2002) had similar range of data as the western springs (yellow symbols). The Valles Caldera Women's Bathhouse spring (WOM) had low [Sr] because the sample was of condensed gases and dissolved strontium is not volatile. The eastern springs are low in both parameters similar to samples collected from the Rio Grande River (blue squares) (Mills, 2003).

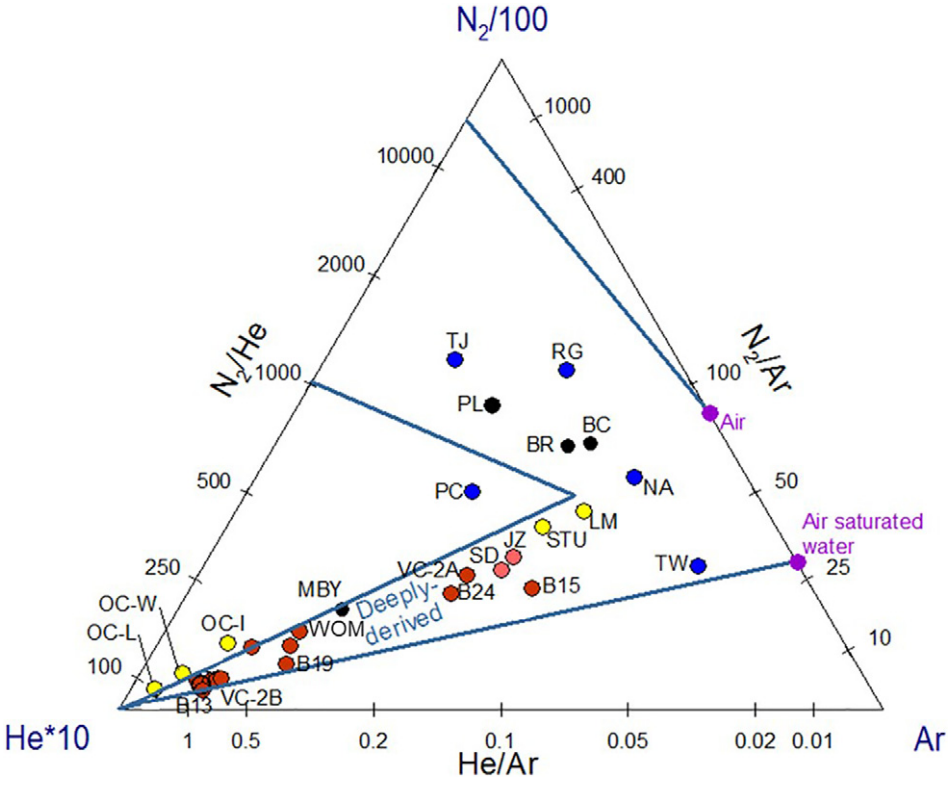

Fig. 8. Dissolved gases of the springs in the study area and free gases of the Valles Caldera (Goff and Janik, 2002; Truesdell and Janik, 1986) are displayed as proportions of Ar-N_2-He to identify mixing trends between helium rich (endogenic) gases and air-like gases. The western springs (yellow symbols) plot along this mixing line with the greatest proportion of helium at Ojo Caliente. All of the eastern springs (black symbols) had excess N_2.

Table 6
Dissolved gases of springs in the study and free gas of the Valles Caldera in volume %.

Sample name	Ar	He	O_2	CO_2	H_2	H_2S	N_2	CH_4	sum	N_2/Ar
Western Rio Grande rift springs										
La Madera Mother spring (a)	1.32	0.07	0.10	7.93	1.03	NA	88.3	0.26	100.0	67.1
La Madera pool (a)	0.57	BDL	14.7	2.16	BDL	NA	82.6	BDL	100.0	145
[b]Ojo Caliente well (a)	0.85	1.35	9.82	2.65	BDL	NA	85.2	0.09	100.0	101
[b]Ojo Caliente Iron spring (a)	0.74	0.66	14.7	0.03	BDL	NA	83.8	0.02	100.0	113
[b]Ojo Caliente Lithium spring (a)	0.54	1.72	6.51	30.7	BDL	NA	60.5	0.05	100.0	111
Statue spring (a)	0.83	0.06	17.4	25.5	BDL	NA	56.2	0.01	100.0	67.8
Eastern Rio Grande rift springs										
Black Rock (a)	0.60	0.02	13.5	0.94	BDL	NA	84.9	BDL	100.0	142
Manby (a)	1.11	0.33	14.7	4.27	BDL	NA	79.5	0.01	100.0	71.7
Bear Crossing (a)	0.80	0.03	17.5	2.00	BDL	NA	79.6	BDL	100.0	99.2
Ponce de Leon (a)	0.84	0.08	16.8	0.02	BDL	NA	82.3	BDL	100.0	97.6
Meteoric Waters in study area										
Big Spring (a)	0.71	0.01	15.7	1.14	BDL	NA	82.4	BDL	100.0	115
Taos Junction (a)	0.79	0.01	17.7	0.08	BDL	NA	81.4	BDL	100.0	103
Rio Grande Spring (a)	0.55	0.01	15.0	1.51	BDL	NA	82.9	BDL	100.0	152
Tusa warm (a)	2.05	0.04	24.4	3.58	BDL	NA	70.0	BDL	100.0	34.2
No Agua (a)	1.14	0.03	15.0	1.47	BDL	NA	82.3	BDL	100.0	72.0
Picuris warm spring (a)	1.24	0.01	14.3	0.37	BDL	NA	84.0	BDL	100.0	67.5
[a]Picuris warm spring (a)	0.73	0.09	14.9	0.91	BDL	NA	83.4	BDL	100.0	113
Valles Caldera springs and wells										
[a]Footbath (b)	0.011	0.012	0.03	97.9	0.48	0.87	0.62	0.064	100.0	56.4
[a]Women bathroom (b)	0.01	0.004	0.0041	98.5	0.1	0.71	0.69	0.016	100.0	69.0
[a]VC-2a well (b)	0.016	0.002	0.0005	97.1	0.25	0.72	0.9	0.017	99.0	58.8
[a]VC-2b well in situ (b)	0.0066	0.0051	0.11	96.9	1.85	0.81	0.29	0.24	100.2	43.9
[a]Baca Well 13 (c)	0.0042	0.0042	NR	99.3	0.0403	0.482	0.142	0.0207	100.0	33.8
[a]Baca Well 13 (c)	0.0058	0.0054	NR	99.2	0.0494	0.534	0.181	0.0244	100.0	31.2
[a]Baca Well 15 (c)	0.027	0.0022	NR	96.7	0.14	1.77	1.13	0.0253	99.8	41.9
[a]Baca Well 19 (c)	0.015	0.0061	NR	98.4	0.106	0.806	0.572	0.0633	100.0	38.1
[a]Baca Well 24 (c)	0.017	0.0016	NR	98.5	0.0542	0.672	0.721	0.018	100.0	42.4
[a]Baca Well 24 (c)	0.013	0.0018	NR	98.4	0.0323	0.778	0.679	0.0085	99.9	52.2
[a]Baca Well 4 (c)	0.0083	0.0067	NR	98.5	0.0645	0.995	0.353	0.0393	100.0	42.5
[a]Tony's spring (b)	0.0081	0.005	0.007	98.8	0.29	0.87	0.62	0.064	100.7	76.5
[a]Mens (b)	0.016	0.0066	0.033	98.3	0.021	0.17	0.89	0.021	99.5	55.6
[a]Main fumerole (b)	0.0055	0.0048	0.0016	99.0	0.044	0.77	0.25	0.033	100.1	45.5
Valles Caldera SW geothermal outflow springs										
[a]Soda Dam (b)	0.02	0.002	0.32	98.4	0.005	0.02	1.10	0.004	99.9	55.0
[a]Jemez spring (b)	0.012	0.0011	0.14	99.1	0.0001	0.063	0.71	0.005	100.0	59.2
[a]"C" Spring (b)	0.05	0.040	0.14	97.7	<0.005	<0.02	1.97	0.004	99.9	39.4

(a) This study; (b) Goff and Janik, 2002; (c) Truesdell and Janik, 1986.
Samples reported in volume % of total gases.
NA - not analyzed.
BDL - Below detection limit.
NR - Not reported.
[a] Free gas.
[b] Sample collected in a vial, water in vial was displaced by bubbles from spring.

used for comparison. The first comparison was with trace element trends. In the plots Cl vs. Li and Cl vs. B, Valles Caldera wells (VC and Baca wells) create a linear chemical trend that Ojo Caliente plots along (Figs. 12A-B). The second comparison was strontium isotope data where the Valles Caldera VC-wells show a similar range in [Sr] as Ojo Caliente and nearly as high of $^{87}Sr/^{86}Sr$ ratios, revealing long water flow through granitic bedrock. The third comparison was demonstrated with two models of varying amounts of ^{3}He and He. Data for these models include dissolved gas data for springs in this study and free and dissovled gas data from the Valles Caldera.

As discussed above, Ojo Caliente had higher [He] and $^{87}Sr/^{86}Sr$ ratios than the other springs in the study area and may reflect long flow pathway through granitic bedrock. To test the idea of a connection between Valles Caldera and Ojo Caliente via a long flow path, [He] was increased by factors of 2 from Valles Caldera values on a plot of CO_2/He vs. R_C/R_A (Fig. 13), which included increasing ^{4}He in the R_C/R_A values. In this model, Ojo Caliente springs plot along the trend of increasing [He]. The interpretation of this plot is that Ojo Caliente waters can be produced from far traveled waters from the Valles Caldera. In a similar model, ^{3}He was exponentially decreased from Valles Caldera values in a plot of $CO_2/^{3}He$ vs. R_C/R_A (^{3}He was also decreased in R_C/R_A values) (Fig. 14), and again Ojo Caliente values generally plot along the modeled lines. In the model of decreasing ^{3}He, La Madera, Statue, and eastern spring samples plot closer to the modeled lines than Ojo Caliente. This is due to greater ^{3}He present in Ojo Caliente samples implying more complex mixing in Ojo Caliente spring waters than only dilution. Further discussion of Ojo Caliente source waters is presented in Section 5.3.

In Figs. 13 and 14, the Ponce de Leon sample plots close to Ojo Caliente samples because of similar $CO_2/^{3}He$ and R_C/R_A values, however Ponce de Leon and Ojo Caliente results show different chemical signatures in all the other figures. Ponce de Leon is part of a non-magmatic geothermal system, causing different chemical signatures than Ojo Caliente. Ponce de Leon is also part of a different geologic setting than Black Rock and Manby, causing different water chemistry among eastern springs. For the purpose of our study, Ponce de Leon provides useful

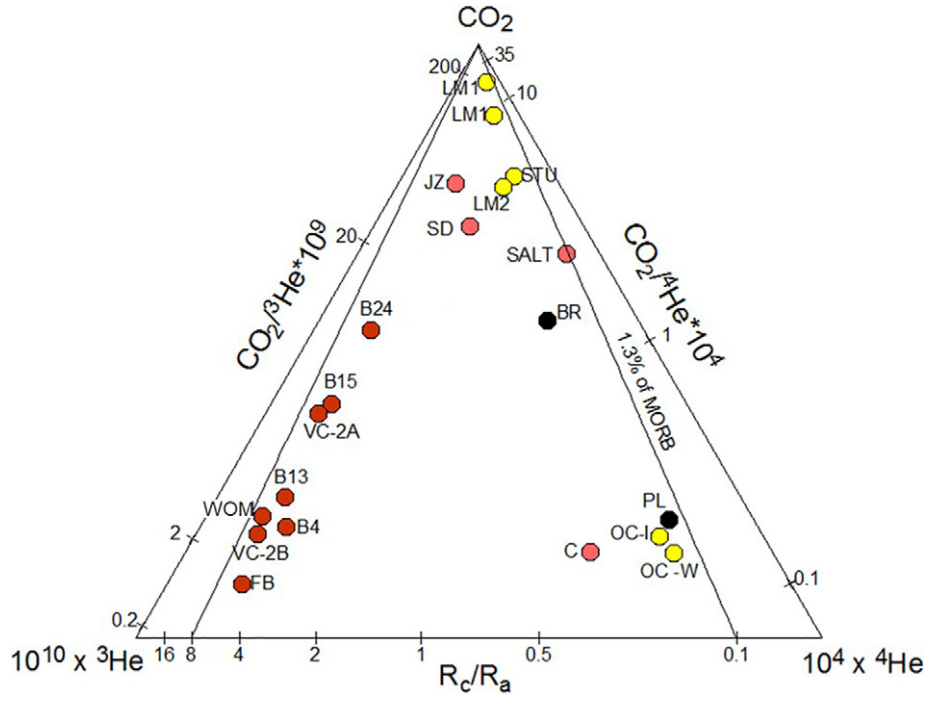

Fig. 9. Trilinear plot of helium isotopes and CO_2. The bottom axis of the trilinear plot is R_C/R_A. Higher R_C/R_A means greater percentage of mantle helium (^3He) and lower R_C/R_A means greater percentage of crustal helium (^4He) (See Section 2.4 "Using a Multiple Tracer Approach" for explanation of R_C/R_A). All of the springs in the study area plot above 0.1 R_A, therefore we conclude mantle degassing from springs occurs throughout the study area. Valles Caldera waters and Valles outflow springs were compiled from Goff and Janik (2002) and Truesdell and Janik (1986).

non-magmatic geothermal data for comparison against Ojo Caliente data.

Simlar to Fig. 14, decreasing ^3He is shown on a plot of $\delta^{13}C_{ext}$ vs. $CO_2/^3He$ (Fig. 15). This decrease is shown as a horizontal trend along the x-axis starting at MORB of 2×10^9 (Marty et al., 1989) and Footbath spring of the Valles Caldera at 1.13×10^9 (Goff and Janik, 2002) and leads to the right. The important observation in Fig. 15 is that Ojo Caliente springs have similar $\delta^{13}C_{ext}$ and $CO_2/^3He$ values as Baca wells 15 and 24.

Data spreading along the $CO_2/^3He$ axis in Figs. 9, 14, and 15 is likely related to the residual component of magmatic degassing (decreasing $CO_2/^3He$ with static or increasing $^3He/^4He$ and $\delta^{13}C\text{-}CO_2$) (Marty and Jambon, 1987; Poreda and Craig, 1989; Poreda et al., 1992, 1993; Dixon et al., 1995; Dixon and Stolper, 1995); and/or mixing with CO_2 evolved from either thermal breakdown of crustal carbonates or degradation of organic matter (Marty and Jambon, 1987; Dixon et al., 1995; Dixon and Stolper, 1995; Tedesco et al., 2010; Darrah et al., 2013); and/or differences in solubilities of CO_2 and He in the magmatic melt (Dixon et al., 1995; Dixon and Stolper, 1995; Tedesco et al., 2010) or crustal fluids (Marty et al., 1989; Gilfillan et al., 2009); and/or He and CO_2 traveling in a gas phase rather than water (Sano et al., 1988; Darrah et al., 2013).

The horizontal trend in Fig. 15 is due to decreasing ^3He, which is especially apparent considering that the absolute abundance of CO_2 is also decreasing from Baca wells 4 and 13 (0.00226 and 0.0034 mol fraction) to Baca wells 15 and 24 (0.0007 and 0.001 mol fraction) (Truesdell and Janik, 1986). Two types of geothermal waters are apparent in the Baca wells based on water chemistry data. Water in Baca wells 4 and 13 was the product of diluting high temperature and high salinity parent water of the Valles Caldera geothermal system with meteoric water, while the water in Baca wells 15 and 24 was the product of conductively cooling Valles Caldera parent water (Truesdell and Janik, 1986).

In summary, evidence of a hydrochemical connection among the Ojo Caliente and the Valles Caldera geothermal systems include: 1) Ojo Caliente springs and Baca wells 15 and 24 have similar range in $\delta^{13}C_{ext}$ and $CO_2/^3He$ ratios, 2) both Ojo Caliente and Valles Caldera waters follow the same trace element trends, 3) Ojo Caliente springs can be modeled from Valles Caldera water by increasing [He] by a factor of 2 and exponentially decreasing ^3He, 4) carbonic nature of the western springs shown with greater concentrations of CO_2, CH_4, HCO_3, C_{ext}, and higher modeled P_{CO2} than the eastern spring group of the RGR. All these findings can be explained by closer proximity to the still-active Valles Caldera geothermal system.

5.3. Estimating percentage of source waters into Ojo Caliente springs

Possible geothermal and/or endogenic sources of Ojo Caliente springs include geothermal input from the Valles Caldera, local magmatism, local non-magmatic far-traveled water, and mantle gases seeping upward along regional faulting. Basic calculations were performed to determine approximate percentages of these sources. It should be noted that because of many possible regional and local end members, these calculations are only conservative estimates. The percentage of Valles Caldera input was determined by dilution of lithium, boron, and CO_2. Dilution was calculated using the average concentration from VC-2A and VC-2B samples (maximum Valles Caldera values) and the average Ojo Caliente concentrations. The results for lithium dilution was 14% and boron was 5%. The difference among the percentages was due to three times more lithium in the Ojo Caliente samples than boron. The concentrations of boron and lithium in the VC wells were comparable. To calculate CO_2 dilution, free gas concentrations from the Valles Caldera were used. A large range of CO_2 concentrations were measured at Ojo Caliente. Dilution was calculated for two Ojo Caliente measurements, 2.65 and 30.72%, compared to the average VC well concentration of 97.0%. The calculated dilution of CO_2 was 31.7 and 2.7%. By using the

Table 7
Dissolved helium isotopes and CO_2.

Sample name	^3He	^4He	CO_2	$CO_2/^3He$ (x 10^9)	Ne	R/R_A	X	R_C/R_A	% Mantle He	Ar	Kr	*Kr/Ar
	pcc/cc	μcc/cc	cc/cc	cc/cc	μcc/cc					μcc/cc	ncc/cc	
Western Rio Grande rift springs												
La Madera Mother spring (a)	3.73	7.99	0.85	229	0.73	0.34	27.4	0.32	4.0	448	65.9	0.000147
La Madera Mother spring (d)	9.08	1.97	0.41	456	0.84	NR	148	0.33	4.1	NR	NR	NR
La Madera pool (a)	8.85	16.3	0.79	89	0.47	0.39	86.9	0.39	4.8	NA	NA	NA
Ojo Caliente Well (a)	57.97	288	0.58	10	8.13	0.14	673	0.14	1.7	2492	459	0.000184
Ojo Caliente Well (e)	30.19	120	NA	NA	0.127	0.2	2372	0.18	2.2	NA	NA	NA
Ojo Caliente iron spring (a)	56.57	257	0.65	11	0.96	0.16	88.6	0.16	2.0	1933	946	0.000489
Statue spring (a)	6.71	18.0	0.86	127	0.95	0.27	47.6	0.26	3.2	596	177	0.000296
Eastern Rio Grande rift springs												
Black Rock (a)	7.90	20.0	0.32	40	7.37	0.28	6.8	0.20	2.5	1140	323	0.000283
Manby (e)	NA	NA	NA	NA	NA	NA	NA	0.32	4.0	NA	NA	NA
Ponce de Leon (a)	20.59	113.57	0.33	16	0.97	0.13	292.3	0.13	1.6	4812	1387	0.000288
Meteoric Waters in study area												
Big spring (a)	6.79	5.63	0.27	40	21.3	0.87	0.7	NA	NA	9442	2658	0.000282
No Agua well (a)	20.8	103	0.46	22	12.2	0.15	21.0	0.12	1.5	NA	NA	NA
Tusa Warm spring (a)	8.29	84.7	0.99	18	18.7	0.95	0.8	NA	NA	NA	NA	NA
Valles Caldera springs and wells												
Footbath Spring (b)*	867	0.012	97.9	1.13	NR	5.16	NR	NR	64.5	110	NR	NR
Womens bath (b)*	345	0.0040	98.5	2.86	NR	6.16	NR	NR	77	100	NR	NR
VC-2a well (b)*	140	0.0020	97.1	6.94	NR	5.0	NR	NR	62.5	160	NR	NR
VC-2b well (b)*	408	0.0051	96.9	2.37	NR	5.72	NR	NR	71.5	66	NR	NR
Baca well 13 (c)	279	0.0042	99.2	3.55	NR	4.75	NR	NR	59.4	14.5	NR	NR
Baca well 15 (c)	128	0.0022	96.7	7.58	NR	4.14	NR	NR	51.8	18.9	NR	NR
Baca well 24 (c)	75.9	0.0016	98.4	13.0	NR	3.93	NR	NR	49.8	18.6	NR	NR
Baca well 4 (c)	362	0.0067	98.5	2.72	NR	3.86	NR	NR	48.3	19.1	NR	NR
Valles Caldera SW geothermal outflow springs												
Soda Dam (b)*	23.5	0.0020	98.4	41.8	NR	0.84	NR	NR	10.5	200	NR	NR
Jemez hot spring (b)*	19.6	0.0011	99.1	50.7	NR	1.27	NR	NR	15.9	120	NR	NR
C spring (b)*	179	0.0400	97.7	5.45	NR	0.32	NR	NR	4	500	NR	NR
Salt Spring (d)	7.4	0.0046	98.4	133	NR	NR	461	0.11	1.4	NR	NR	NR
Tierra Amarilla												
Twin Mounds (d - labeled Grassy spring)	23.5	84.7	0.986	42	0.00	NA	958	0.198	2.5	NR	NA	NA
Other regional springs of interest												
Chimayo Well (b)*	43.7	0.0048	99.6	22.8	NR	0.65	NR	NR	8.1	50	NR	NR

(a) This study; (b) Goff and Janik, 2002; (c) Truesdell and Janik, 1986; (d) Newell at al., 2005; (e) unpublished Crossey.
*Data from Goff and Janik (2002) is dry gas in mol%.
Samples from the study site were analyzed from gases exolved from water in copper tubes.
He/Ne of air used to correct measured R/R_A is 0.4.
$X = (He/Ne)_m / (He/Ne)_{air.}$
$R_C/R_A = (R/R_A * X - 1) / (X - 1)$.
NA - Not analyzed.
NR - Not reported.
*$^{84}Kr/^{36}Ar$ Air values are 0.0207 (Moreira et al., 1998).

Table 8
Saturation indexes.

Sample name	SI - Calcite	SI - Dolomite	SI - Gypsum	SI - CO_2(g)
Western Rio Grande rift springs				
LM1 mother spring	−0.89	−1.85	−1.14	0.02
LM 2 Pool by HWY	−0.5	−1.08	−1.10	−0.22
Ojo Caliente Well	−0.17	−0.31	−2.34	−0.19
Ojo Caliente Lithium spring	−0.17	−0.26	−2.27	−0.33
Ojo Caliente Iron spring	−0.28	−0.51	−2.31	−0.27
Statue spring	−0.84	−1.73	−1.18	0.04
Eastern Rio Grande rift springs				
Black Rock	−0.35	−0.90	−1.96	−2.09
Manby	−0.63	−1.52	−1.93	−1.62
Bear Crossing	−0.56	−1.4	−2.97	−2.70
Ponce de Leon	0.15	−0.46	−2.22	−3.64
Meteoric Waters in study area				
Taos Junction	−0.02	−0.75	−2.85	−2.52
No Agua	−0.89	−2.06	−3.37	−1.86
Tusa warm	−0.56	−1.73	−3.65	−2.22
Picuris warm	−4.08	−8.52	−3.99	−1.05

Saturation indices (SI) were modeled in PHREEQC Version 2.

conservative estimates, about 3 to 5% of Ojo Caliente water was sourced from the Valles Caldera geothermal system.

Radiogenic strontium ratios were used to calculate the amount of locally derived geothermal waters. As discussed in Section 2.4, the $^{87}Sr/^{86}Sr$ ratio reflects water rock interaction along flow pathways (Faure, 1986). The local non-magmatic geothermal influence on strontium ratios was calculated using the Ponce de Leon strontium ratio, 0.713287, compared with locally measured minimum and maximum ratios. The local minimum ratio was the New Mexican Paleozoic limestone of 0.709 (Crossey et al., 2006) and the maximum ratio was the Precambrian basement from Rocky Mountain National Park of 0.740 (Clow et al., 1997). By using these values for comparison, the calculated influence of basement rock at Ponce de Leon was about 13%. Ojo Caliente radiogenic strontium ratios were comparable to the local maximum value. We interpret that the locally non-magmatic geothermal impact on Ojo Caliente waters was likely similar to Ponce de Leon; therefore, the impact was about 13% of the total geothermal influence.

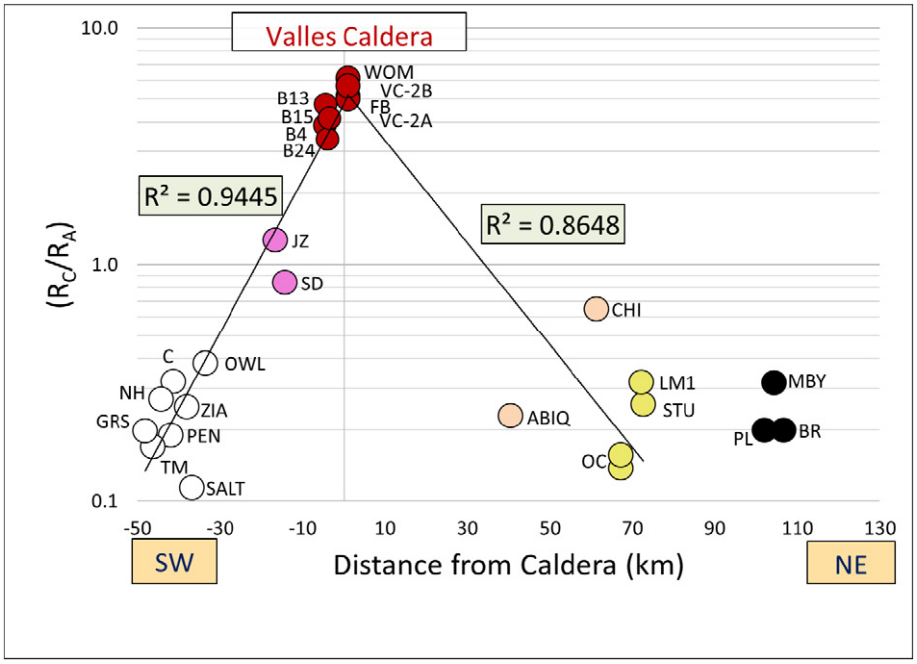

Fig. 10. R_C/R_A plotted against distance from the Valles Caldera. Springs from the Valles Caldera to the southwest are shown as negative values on the x-axis and springs to the northeast are positive values. Exponential trends of decreasing R_C/R_A with distance from the Valles Caldera to the southwest are apparent, however trends are not as apparent to the northeast, therefore this study compared spring water chemistries of opposite sides of the northern RGR to study anomalies in the western spring group. Abiquiú spring (ABIQ) and Chimayó (CHI) springs are shown as peach symbols (Goff and Janik, 2002) and are shown to demonstrate large scale trends; they are not part of either the western or eastern spring groups and are therefore not presented on previous figures. White symbols are the San Ysidro springs (Newell et al., 2005; McGibbon et al., 2018). Red symbols are the Valles Caldera springs and wells (Goff and Janik, 2002; Goff and Gardner, 1994). Pink symbols are Soda Dam and Jemez springs of the Valles Caldera geothermal outflow plume waters (Goff and Janik, 2002).

Detected methane in Ojo Caliente samples suggests there is a magmatic source due to high temperature synthesis reactions of CO_2 and H_2 (Welhan, 1988). Methane concentrations from Ojo Caliente samples were mostly the same order of magnitude as the Baca and VC well samples. Considering significant dilution of Valles Caldera solutes and gases, as demonstrated above, methane detections are interpreted to be locally derived, because diluted methane from the Valles Caldera would likely not be detectable in Ojo Caliente spring water. The only local magmatism in the region of Ojo Caliente is partially melted mantle along the Jemez lineament. An estimated percentage of this source is unclear, however is likely small.

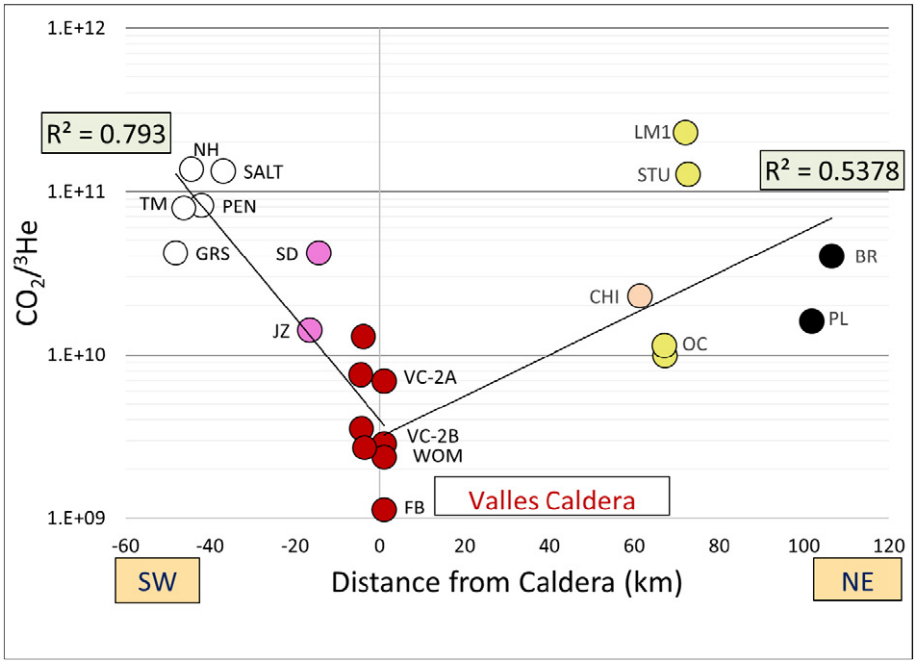

Fig. 11. $CO_2/^3He$ plotted against distance from the Valles Caldera. The same symbols are used here as Fig. 10.

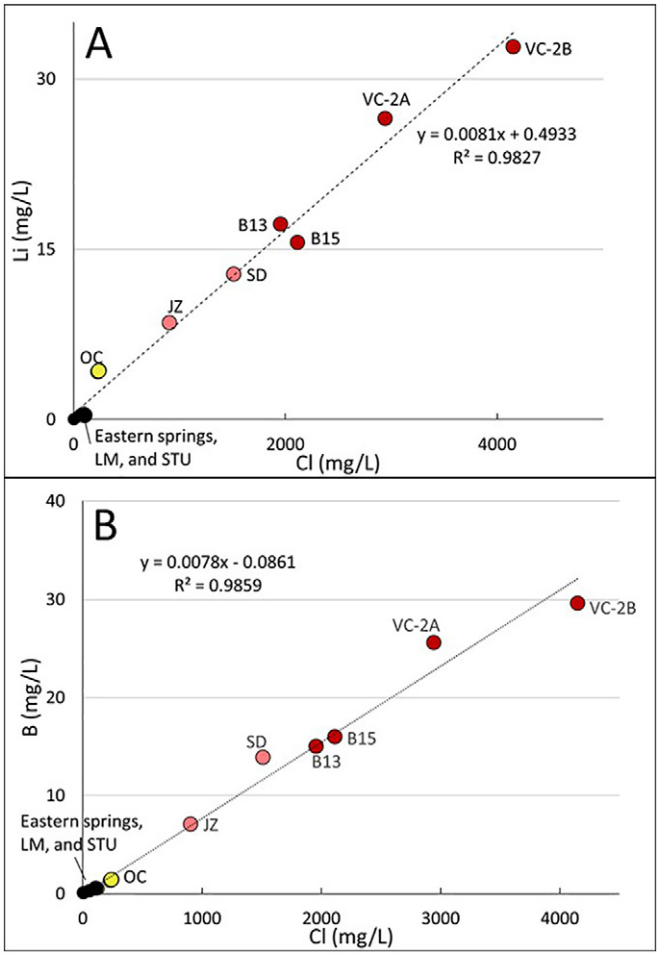

Fig. 12. Cross plots and linear regressions of geothermal-associated trace element concentrations (Li, B). (A) Ojo Caliente had the highest [Li] among the springs in the study area and lies along a trend line created by the Valles Caldera well waters. (B) the plot with [B] shows similar trends as [Li].

Calculating contributions of mantle helium sourced either from the Valles Caldera or regional degassing is obscure, because R_C/R_A results were similar among Ojo Caliente and eastern RGR spring samples. By using dilution calculations above, R_C/R_A in Ojo Caliente samples is 3% diluted Valles Caldera waters. However, given similar values in eastern springs, the mantle helium in Ojo Caliente may instead be regional degassing. Dilution of Valles Caldera water and gases is better estimated by the solutes and CO_2 described above.

In summary, diluted input of the Valles Caldera solutes and gases is approximately 3 to 5%, local non-magmatic geothermal input is about 13%, and a small contribution of local magmatism from partially melted mantle along the Jemez lineament. The remaining spring waters are meteoric, which is consistent with oxygen and hydrogen isotope results discussed in Section 4.

5.4. Silica and Na-K-Ca geothermometers

To gain further insight into spring water origins, the silica and Na-K-Ca geothermometers were calculated. The silica geothermometer calculation was from Fournier (1977) for adiabatic cooling with maximum steam loss. The Na-K-Ca geothermometer calculation was based on Fournier and Truesdell (1973) using a β value of 1.33 as determined by preliminary calculations shown in Table 9 (Fournier and Truesdell, 1973). The silica geothermometer is a standard tool used in geothermal studies. The Na-K-Ca geothermometer was used because it was created for samples with high concentration of calcium and cold to slightly thermal spring water (Fournier and Truesdell, 1973), both are representative features of our studied springs.

For the Ojo Caliente samples, the calculated silica geothermometer equilibration temperatures were 107 to 110 °C and the Na-K-Ca geothermometer temperatures were 179 to 191 °C (Table 9). Even using the higher estimates, the calculated temperatures are below the measured temperatures from the Baca and VC wells, which ranged from 210 to 295 °C. The La Madera, Statue, and Ponce de Leon equilibration temperatures for both equations ranged from 65 to 106 °C; the difference in the temperatures among the geothermometers was 3 to 20 °C. Generally, the Na-K-Ca geothermometer calculated higher temperatures.

Geothermometetry was performed for Ojo Caliente samples in Vuataz et al. (1984) and similar temperatures were calculated. Vuataz et al. (1984) determined which mineral phases participated in water-rock interactions for Ojo Caliente spring water, which were silica minerals, clays, carbonates, fluorite, and sulfates. These minerals are consistent with primary minerals of the metarhyolite that Ojo Caliente springs discharge through (Vuataz et al., 1984). They concluded that Ojo Caliente spring waters are mainly the result of low-temperature reactions. Similarly, on the silica solubility curves presented in Fournier and Rowe (1966), Ojo Caliente samples plot near the amorphous silica curve, indicating more surficial reactions, such as dissolving amorphous silica deposits near the ground surface (Fournier and Rowe, 1966). The geothermometer data illustrates that low temperature reactions dominate the spring water chemistry, confirming that the endogenic components were found at trace concentrations.

5.5. Discussion: local CO_2 variation among the western spring group

Large travertine deposits at La Madera and minor travertine deposits at Ojo Caliente are significant because they suggest a nearby reservoir of deeply sourced CO_2. Higher CO_2 concentrations were measured in La Madera/Statue spring samples as well as other indicators of CO_2 equilibration compared to Ojo Caliente. A lower pH was measured from La Madera at 6.0 compared to Ojo Caliente at 6.6. Higher P_{CO2} was measured at La Madera at $10^{0.03}$ compared to Ojo Caliente at $10^{-0.26}$. Lastly, higher calcite saturation index at La Madera was measured at −0.8 compared Ojo Caliente at −1.07. These differences among La Madera and Ojo Caliente are likely structurally related. Future work is needed to understand the structures causing greater CO_2 degassing at La Madera.

6. Conclusions

Due to the complex hydrogeology of geothermal systems, this work used geochemistry to study the origins of spring waters in northern New Mexico. Based on major ion chemistry, trace elements, gas abundance, carbon, strontium, and helium isotopes, we conclude that there are distal influences of the Valles Caldera geothermal system in Ojo Caliente spring waters.

Rough estimates of geothermal source contributions into Ojo Caliente spring water were calculated. We conclude that about 3 to 5% of Ojo Caliente spring water chemistry can be explained by a large advection system sourced from the Valles Caldera. Though 3 to 5% is a small contribution, significant permeability along fault networks is required, and therefore high permeability is demonstrated by this study. In addition to a large advection system, we calculated about 13% input of non-magmatic deeply circulated fluids. Ojo Caliente springs also had methane detections, unlike eastern springs, suggesting a local magmatic source (Welhan, 1988), which we interpret to be from the Jemez lineament. The Jemez lineament passes through the entire study site, to explain the unique chemistry at Ojo Caliente, we suggest greater permeability along Ojo Caliente faults allowing upward mobility of gases.

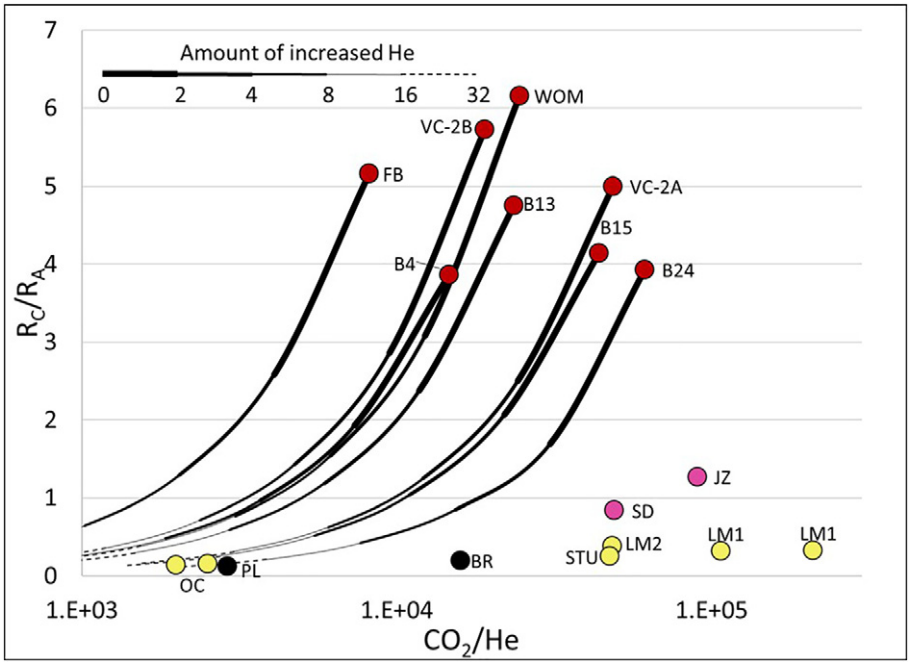

Fig. 13. Model of decreasing He ($^3He/^4He$ is expressed as R_C/R_A). The curved lines are a model of increasing [He] by factors of 2, including increasing ^4He in the R_C/R_A values. This model was created by starting with free and dissolved gas data from Valles Caldera samples and then exponentially increasing [He]. Ojo Caliente springs plot along the modeled lines revealing a possible connection with the Valles Caldera. Greater [He] in Ojo Caliente samples compared to La Madera and Statue springs account for the large spread of CO_2/He data in the western springs (yellow symbols). Valles Caldera and related outflow springs were compiled from Goff and Janik (2002) and Truesdell and Janik (1986).

Lastly, the majority of the water is of meteoric origins. The mixture of these sources is illustrated in Fig. 16.

In our model of migrating constituents of the Valles Caldera, we propose that the fluid and gases originate from great depths below the ground surface, possibly near the magma body, rather than a shallow outflow plume of Valles Caldera geothermal waters. The Valles Caldera magma body was imaged at 4.7 km (Nielson and Hulen, 1984) to 7 km below the ground surface Aprea et al. (2002), which provides a significant vertical distance to allow fluids and volatiles to migrate great distances laterally. High temperatures and pressures of the Valles Caldera can cause this migration, as seen by well temperatures and pressures of 210 to 290 °C (Goff and Janik, 2002) and 140 to 152 psi

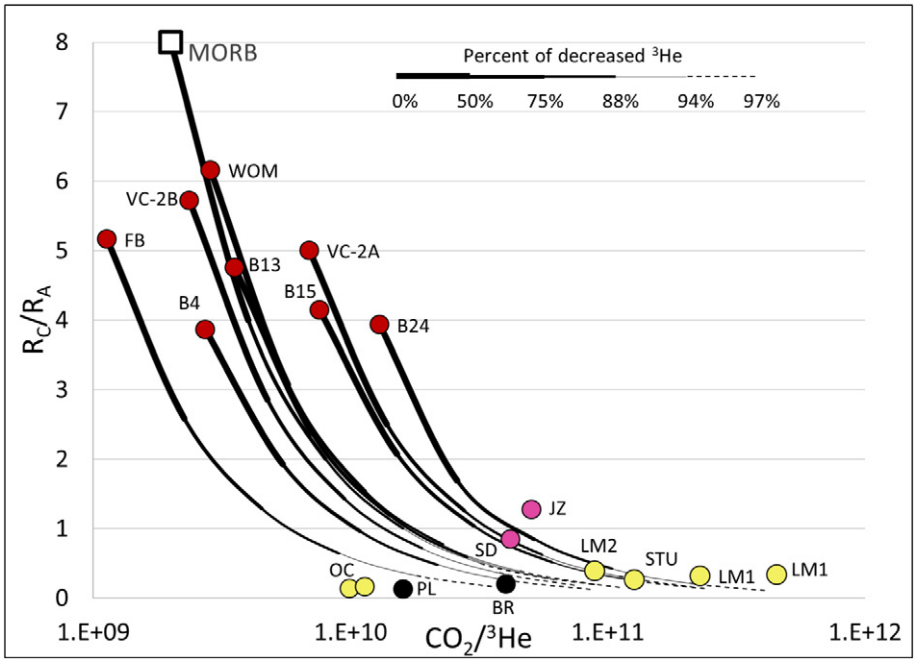

Fig. 14. Model of decreasing ^3He ($^3He/^4He$ is expressed as R_C/R_A). Similar to Fig. 13, the curved lines represent a model of decreasing ^3He from Valles Caldera samples and MORB. Ojo Caliente plots near the modeled lines. Greater ^3He concentrations in Ojo Caliente samples compared to La Madera and Statue springs cause Ojo Caliente samples to plot further to the left. Valles Caldera and related outflow springs were compiled from Goff and Janik (2002) and Truesdell and Janik (1986).

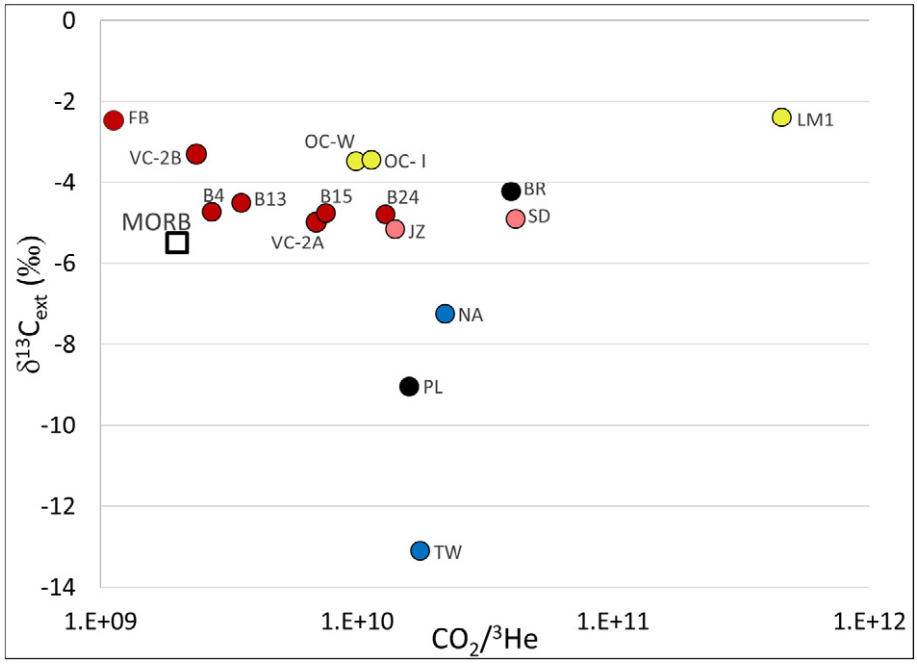

Fig. 15. $\delta^{13}C_{ext}$ vs. $CO_2/^3He$. Valles Caldera samples plot close to MORB ($CO_2/^3He = 2 \times 10^9$) and along a horizontal trend from MORB to the right. This horizontal trend from Baca wells 4 and 13 to Baca wells 15 to 24 is from decreasing ^3He because CO_2 is also decreasing according to dissolved gas data from Truesdell and Janik (1986). It is notable that Ojo Caliente $CO_2/^3He$ values overlap with values from Baca wells 15 and 24. The springs with lighter $\delta^{13}C_{ext}$ values are Ponce de Leon (PL) and meteoric waters (blue symbols).

(White et al., 1984). Fig. 16 illustrates the depths of source fluids and gases.

Considering that the Valles Caldera magma body is within crystalline bedrock, fault network permeability is the primary path for migration. Permeability in well-developed damaged zones along thin regions parallel to fault zones have significant permeability (Evans et al., 1997). Faults have been shown to be conduits for fluid and gas transport (Mailloux et al., 1999; Easley and Morgan, 2013; Karlstrom et al., 2013; Fischer and Chiodini, 2015; Lee et al., 2016), and fault intersections provide conduits for pristine mantle gases (de Moor et al., 2013). The spring chemistry of this study demonstrated that the Jemez lineament, regional faulting, extensional features, and crustal thinning provided sufficient permeability for fluid and gas migration. As a secondary study to this paper, a permeability test studying CO_2 seepage or conductivity along the Embudo and Ojo Caliente faults would be beneficial.

This study stressed that faults allow for transport of endogenic fluids in tectonically active regions. Our results demonstrate the importance of studying trace fluid and gas chemistry as it provides insight into the extent of regional geothermal influence. Continued reassessment is needed to fully understand large scale fault networks in relation to gas transport mechanisms.

Acknowledgments

We are grateful for the lab facilities and advisement from Mehdi Ali of the Chemistry Laboratory at UNM, Yemane Asmerom and Victor Polyak of the Radiogenic Isotope Laboratory of UNM, and Viorel Atudorei and Laura Berkemper of the Center of Stable Isotope Laboratory at UNM. We thank Hyunwoo Lee of the University of New Mexico for helping collect gas samples, analyzing samples and advising on gas chemistry. We thank Paul Bauer for helpful discussion of springs of the Taos region. We are grateful for the land owners of La Madera and Ojo Caliente for permission to access their land. We gratefully acknowledge funding from National Science Foundation (NSF) EPSCOR award

Table 9
Geothermometer results.

Sample name	Si (mg/L)	SiO_2 (mg/L)	[a]Silica geothermometer equilibrated temperatures (°C)	[b]β detemination (=log($Ca^{1/2}$/Na) + 2.06)	[c]Na-K-Ca geothermometer equilibrated temperatures (°C)
Western Rio Grande rift springs					
La Madera Mother spring	9.23	19.8	68.5	2.9	82.0
La Madera pool	8.35	17.9	65.2	2.9	85.4
Ojo Caliente Well	28.2	60.4	110	1.8	192
Ojo Caliente Lithium spring	26.7	57.1	107	1.8	180
Ojo Caliente Iron spring	27.6	59.1	109	1.8	186
Statue spring	9.43	20.2	69.2	3.0	72.6
Eastern Rio Grande rift springs					
Ponce de Leon	25.6	54.8	106	2.5	87.8

[a] Temperature = $(1522/(5.75 - \log(SiO_2))) - 273.15$ (Fournier, 1977).
[b] Postive values indicate that 1.3 should be used for β (Fournier and Truesdell, 1973).
[c] Temperature = $(1647/(\log(Na/K) + \beta(\log(\sqrt{Ca})/Na) + 2.24)) - 273.15$ (Fournier and Truesdell, 1973).

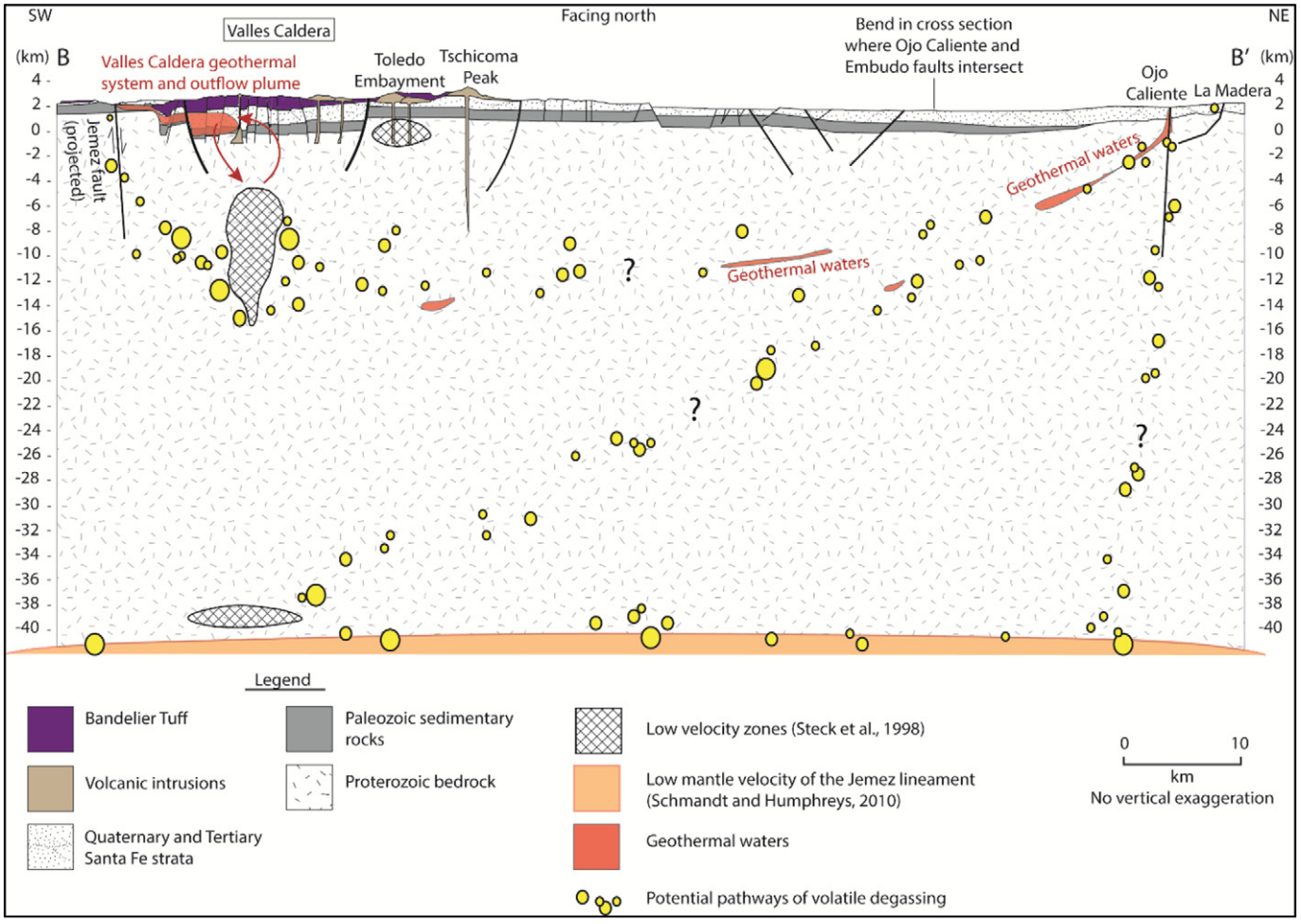

Fig. 16. Southwest-northeast cross section from the Valles Caldera to the western spring group along the hypothesized Embudo fault zone flow path and schematic drawing of volatile degassing. A CO_2 souce for Ojo Caliente waters may be from magma chambers associated with the Valles Caldera. Transport could be along shown faults, through the Paleozoic aquifers (gray), brittle ductile transition (about 6–8 km below the ground surface), or via pathways from the mantle. This cross section is parallel to the Jemez lineament and Embudo fault zone. The convecting geothermal waters of the Valles Caldera are shown flowing to the southwest and discharging along the Jemez fault (projected). The magma body locations were interpreted from Steck et al. (1998). The cross section was adapted from Goff et al. (2014), Koning et al. (2011), May (1984), and maps from the New Mexico Bureau of Geology including the Valles Caldera cross section by Goff et al. (2011), and the Vallecitos (Kempter et al., 2005), Chili (Koning et al., 2005b), and Ojo Caliente (Koning et al., 2005a) Quadrangle maps.

#IIA-1301346 and a student research grant from New Mexico Geological Society.

Appendix A. Supplementary data

Supplementary data to this article can be found online at https://doi.org/10.1016/j.jvolgeores.2019.106663.

References

Andrews, J.N., 1985. The isotopic composition of radiogenic helium and its use to study groundwater movements in confined aquifers. Chem. Geol. 49 (1), 339–351. https://doi.org/10.1016/0009-2541(85)90166-4.

Appelt, R.M., 1998. $^{40}Ar/^{39}Ar$ Geochronology and Volcanic Evolution of the Taos Plateau Volcanic Field, Northern New Mexico and Southern Colorado. M.S. thesis. New Mexico Institute of Mining and Technology, Socorro, NM.

Aprea, C.M., Hildebrand, S., Fehler, M., Steck, L., 2002. Three-dimensional Kirchhoff migration: Imaging of the Jemez volcanic field using teleseismic data. J. Geophys. Res. 107 (B10, 2247), 1–15. https://doi.org/10.1029/2000JB000097.

Ballentine, C.J., Burgess, R., Marty, B., 2002. Tracing fluid origin, transport and interaction in the crust. Noble Gases in Geochemistry and Cosmochemistry 47, 539–614. https://doi.org/10.2138/rmg.2002.47.13.

Barry, P.H., Hilton, D.R., Furi, E., Halldorsson, S.A., Gronvold, K., 2014. Carbon isotope and abundance systematics of Icelandic geothermal gases, fluids and subglacial basalts with implications for mantle plume-related CO_2 fluxes. Geochim. Cosmochim. Acta 134, 74–99. https://doi.org/10.1016/j.gca.2014.02.038.

Bauer, P., Kelson, K., 2004. Cenozoic Structural Development of the Taos Area. vol. 55. New Mexico Geological Society, Guidebook, pp. 129–146.

Cartwright, I., Weaver, T., Tweed, S., Ahearne, D., Cooper, M., Czapnik, K., Tranter, J., 2002. Stable isotope geochemistry of cold CO_2-bearing mineral spring waters, Daylesford, Victoria, Australia: sources of gas and water and links with waning volcanism. Chem. Geol. 185 (1), 71–91. https://doi.org/10.1016/S0009-2541(01)00397-7.

Chafetz, H.S., Folk, R.L., 1984. Travertines: depositional morphology and the bacterially constructed constituents. J. Sediment. Res. 54 (1), 289–316.

Chiodini, G., Cardellini, C., Amato, A., Boschi, E., Caliro, S., Frondini, F., Ventura, G., 2004. Carbon dioxide earth degassing and seismogenesis in central and southern Italy. Geophys. Res. Lett. 31 (7), 2–5. https://doi.org/10.1029/2004GL019480.

Clarke, W.B., Beg, M.A., Craig, H., 1969. Excess 3He in the sea: evidence for terrestrial primordial helium. Earth Planet. Sci. Lett. 6 (3), 213–220. https://doi.org/10.1016/0012-821X(69)90093-4.

Clarke, W.B., Jenkins, W.J., Top, Z., 1976. Determination of tritium by mass spectometric measurement of ^3He. The International Journal of Applied Radiation and Isotopes 27 (9), 515–522. https://doi.org/10.1016/0020-708X(76)90082-X.

Clow, D.W., Mast, M.A., Bullen, T.D., Turk, J.T., 1997. Strontium 87/strontium 86 as a tracer of mineral weathering reactions and calcium sources in an alpine/subalpine watershed, Loch Vale, Colorado. Water Resour. Res. 33 (6), 1135–1351. https://doi.org/10.1029/97WR00856.

Cordell, L., 1978. Regional geophysical setting of the Rio Grande rift. GSA Bull. 89 (7), 1073–1090. https://doi.org/10.1130/0016-7606(1978)89<1073:RGSOTR>2.0.CO;2.

Craig, H., 1953. The geochemistry of the stable carbon isotopes. Geochim. Cosmochim. Acta 3 (2–3), 53–92. https://doi.org/10.1016/0016-7037(53)90001-5.

Craig, H., 1977. Isotopic geochemistry and hydrology of geothermal waters in the Ethiopian Rift Valley. United Nations Technical Report SIO Reference, pp. 1–147.

Craig, H., Lupton, J.E., 1976. Primordial neon, helium, and hydrogen in oceanic basalts. Earth Planet. Sci. Lett. 31 (3), 369–385. https://doi.org/10.1016/0012-821X(76)90118-7.

Crossey, L.J., Fischer, T.P., Patchett, P.J., Karlstrom, K.E., Hilton, D.R., Newell, D.L., Huntoon, P., de Leeuw, G.A.M., 2006. Dissected hydrologic system at the Grand Canyon: Interaction between deeply derived fluids and plateau aquifer waters in modern springs and travertine. Geology 34 (1), 25–28. https://doi.org/10.1130/G22057.1.

Crossey, L.J., Karlstrom, K.E., Springer, A.E., Newell, D., Hilton, D.R., Fischer, T., 2009. Degassing of mantle-derived CO_2 and He from spring in the Southern Colorado Plateau region – Neotectonic connections and implications for groundwater systems. GSA Bull. 121 (7–8), 1034–1053. https://doi.org/10.1130/B26394.1.

Crossey, L.J., Karlstrom, K.E., Newell, D.L., Kooser, A., Tafoya, A., 2011. The La Madera Travertines, Rio Ojo Caliente, Northern New Mexico: Investigating the Linked System of CO2-Rich Springs and Travertines as Neotectonic and Paleoclimate Indicators. vol. 62. New Mexico Geological Society, Guidebook, pp. 301–316.

Crossey, L.J., Karlstrom, K.E., Schmandt, B., Crow, R.R., Colman, D.R., Cron, B., Takacs-Vesbach, C.D., Dahm, C.N., Northup, D.E., Hilton, D.R., Ricketts, J.W., Lowry, A.R., 2016. Continental smokers couple mantle degassing and distinctive microbiology within continents. Earth Planet. Sci. Lett. 435, 22–30. https://doi.org/10.1016/j.epsl.2015.11.039.

Darrah, T.H., Tedesco, D., Tassi, F., Vaselli, O., Cuoco, E., Poreda, R.J., 2013. Gas chemistry of the Dallol region of the Danakil Depression in the Afar region of the northern-most East African Rift. Chem. Geol. 339, 16–29. https://doi.org/10.1016/j.chemgeo.2012.10.036.

Darrah, T.H., Vengosh, A., Jackson, R.B., Warner, N.R., Poreda, R.J., 2014. Noble gases identify the mechanisms of fugitive gas contamination in drinking-water wells overlying the Marcellus and Barnett Shales. Proc. Natl. Acad. Sci. 111 (39), 14076–14081. https://doi.org/10.1073/pnas.1322107111.

De Muynck, D., Huelga-Suarez, G., Van Heghe, L., Degryse, P., Vanhaecke, F., 2009. Systematic evaluation of a strontium-specific extraction chromatographic resin for obtaining a purified Sr fraction with quantitative recovery form complex and Ca-rich matrices. J. Anal. At. Spectrom. 24 (11), 1498–1510. https://doi.org/10.1039/B908645E.

Deines, P., Langmuir, D., Harmon, R.S., 1974. Stable carbon isotope ratios and the existence of a gas phase in the evolution of carbonate ground waters. Geochim. Cosmochim. Acta 38 (7), 1147–1164. https://doi.org/10.1016/0016-7037(74)90010-6.

Dixon, J.E., Stolper, E.M., 1995. An experimental study of water and carbon dioxide solubilities in mid-ocean ridge basaltic liquids .2. Applications to degassing. J. Petrol. 36 (6), 1633–1646. https://doi.org/10.1093/oxfordjournals.petrology.a037268.

Dixon, J.E., Stolper, E.M., Holloway, J.R., 1995. An experimental study of water and carbon dioxide solubilities in mid ocean ridge basaltic liquids .1. Calibration and solubility models. J. Petrol. 36 (6), 1607–1631. https://doi.org/10.1093/oxfordjournals.petrology.a037267.

Drakos, P., Sims, K., Riesterer, J., Blusztajn, J., Lazarus, J., 2004. Chemical and isotopic constraints on source-waters and connectivity of basin-fill aquifers in the southern San Luis basin, New Mexico. New Mexico Geological Society, Guidebook. vol. 55, pp. 405–414.

Drever, J.I., 1997. The Geochemistry of Natural Waters. 2nd edition. Prentice Hall.

Easley, E., Morgan, P., 2013. Fluid, gas, and isotopic variation of thermal springs in the Southern Rocky Mountains: Colorado. GRC Transactions 37, 385–391.

Easley, E., Garchar, L., Bennett, M., Morgan, P., Wendlandt, R.F., 2011. A geochemical and isotopic study of two geothermal prospects in the Rio Grande Rift, Colorado and New Mexico. Mt. Geol. 48 (4), 95–106.

Ellis, A.J., Mahon, W.A.J., 1977. Chemistry and Geothermal Systems. Academic Press.

Evans, J.P., Forster, C.B., Goddard, J.V., 1997. Permeability of fault-related rocks, and implications for hydraulic structure of fault zones. J. Struct. Geol. 19 (11), 1393–1404. https://doi.org/10.1016/S0191-8141(97)00057-6.

Evans, W.C., Bergfeld, D., van Soest, M.C., Huebner, M.A., Fitzpatrick, J., Revesz, K.M., 2006. Geochemistry of low-temperature springs northwest of Yellowstone caldera: seeking the link between seismicity, deformation, and fluid flow. J. Volcanol. Geotherm. Res. 154 (3), 169–180. https://doi.org/10.1016/j.jvolgeores.2006.01.001.

Faure, G., 1986. Principles of Isotope Geology. 1st edition. Wiley, New York (75 p.).

Fischer, T.P., Chiodini, G., 2015. Volcanic, magmatic and hydrothermal gases. The Encyclopedia of Volcanos (Chapter 35).

Fontes, J.C., Garnier, J.M., 1979. Determination of the initial ^{14}C activity of the total dissolved carbon: a review of the existing models and a new approach. Water Resour. Res. 15 (2), 399–413. https://doi.org/10.1029/WR015i002p00399.

Fournier, R.O., 1977. Chemical geothermometers and mixing models for geothermal systems. Geothermics 5 (1–4), 41–50. https://doi.org/10.1016/0375-6505(77)90007-4.

Fournier, R.O., Rowe, J.J., 1966. Estimation of underground temperatures from the silica content of water from hot springs and wet-steam wells. Am. J. Sci. 264, 685–697. https://doi.org/10.2475/ajs.264.9.685.

Fournier, R.O., Truesdell, A.H., 1973. An empirical Na-K-Ca geothermometer for natural waters. Geochim. Cosmochim. Acta 37, 1255–1275. https://doi.org/10.1016/0016-7037(73)90060-4.

Gardner, J.N., Goff, F.E., 1984. Potassium-argon dates from the Jemez volcanic field – Implications for tectonic activity in the north-Central Rio Grande rift. N. M. Geol. Soc. Guideb. 35, 75–81.

Gerlach, T.M., Taylor, B.E., 1990. Carbon isotope constraints on degassing of carbon dioxide from Kilauea Volcano. Geochim. Cosmochim. Acta 54 (7), 2051–2058. https://doi.org/10.1016/0016-7037(90)90270-U.

Giggenbach, W.F., 1992. The composition of gases in geothermal and volcanic systems as a function of tectonic setting. Water-Rock Interaction. vol. 2, pp. 873–878.

Gilfillan, S.M., Ballentine, C.J., Holland, G., Blagburn, D., Sherwood Lollar, B., Stevens, S., Schoell, M., Cassidy, M., 2008. The noble gas geochemistry of natural CO2 gas reservoirs from the Colorado Plateau and Rocky Mountain provinces, USA. Geochim. Cosmochim. Acta 72 (4), 1174–1198. https://doi.org/10.1016/j.gca.2007.10.009.

Gilfillan, S.M.V., Sherwood Lollar, B., Holland, G., Blagburn, D., Stevens, S., Schoell, M., Cassidy, M., Ding, Z.J., Zhou, Z., Lacrampe-Couloume, G., Ballentine, C.J., 2009. Solubility trapping in formation water as dominant CO2 sink in natural gas fields. Nature 458, 614–618. https://doi.org/10.1038/nature07852.

Goff, F., Gardner, J., 1994. Evolution of a mineralized geothermal system, Valles Caldera, New Mexico. Econ. Geol. 89 (8), 1803–1832. https://doi.org/10.2113/gsecongeo.89.8.1803.

Goff, F., Janik, C.J., 2002. Gas geochemistry of the Valles caldera region, New Mexico and comparisons with gases at Yellowstone, Long Valley and other geothermal systems. J. Volcanol. Geotherm. Res. 116 (3), 229–323. https://doi.org/10.1016/S0377-0273(02)00222-6.

Goff, F., McMurtry, G.M., Counce, D., Simac, J.A., Roldan-Manzo, A.R., Hilton, D.R., 2000. Contrasting hydrothermal activity at Sierra Negra and Alcedo volcanos, Galapagos Archipelago, Ecuador. Bull. Volcanol. 62 (1), 34–52. https://doi.org/10.1007/s004450050289.

Goff, F., Gardner, J.N., Reneau, S.L., Kelley, S.A., Kempter, K.A., Lawrence, J.R., 2011. Geologic Map of the Valles Caldera, Jemez Mountains, New Mexico. New Mexico Bureau of Geology and Mineral Resources, New Mexico Institute of Mining and Technology.

Goff, F., Warren, R.G., Goff, C.J., Dunbar, N., 2014. Eruption of reverse-zoned upper Tshirege Member, Bandelier Tuff from centralized vents within Valles caldera, New Mexico. J. Volcanol. Geotherm. Res. 276, 82–104. https://doi.org/10.1016/j.jvolgeores.2014.02.018.

Grauch, V.J.S., Keller, G.R., 2004. Gravity and aeromagnetic expression of tectonic and volcanic elements of the southern San Luis basin, New Mexico and Colorado. New Mexico Geological Society, Guidebook. vol. 55, pp. 230–243.

Griesshaber, E., O'Nions, R.K., Oxburgh, E.R., 1992. Helium and carbon isotope systematics in crustal fluids from the Eifel, the Rhine Graben and Black Forest, FRG. Chem. Geol. 99 (4), 213–235. https://doi.org/10.1016/0009-2541(92)90178-8.

Gupta, P., Noone, D., Galewsky, J., Sweeney, C., Vaughn, B.H., 2009. Demonstration of high-precision continuous measurement of water vapor isotopologues in laboratory and remote field deployments using wavelength-scanned cavity in-down spectroscopy (WS-CRDS) technology. Rapid Commun. Mass Spectrom. 23 (16), 2534–2542. https://doi.org/10.1002/rcm.4100.

Hautman, D.P., Munch, D.J., 1997. Method 300.1 Determination of Inorganic Anions in Drinking Water by Ion Chromatography, Revsion 1.0. National Exposure Research Laboratory Office of Research and Development U.S. Environmental Protection Agency Cincinnati, OH, p. 45268.

Hilton, D., 1996. The helium and carbon isotope systematics of a continental geothermal system: results from monitoring studies at Long Valley caldera (California, U.S.A.). Chem. Geol. 127 (4), 269–295. https://doi.org/10.1016/0009-2541(95)00134-4.

Hogan, J.F., Phillips, F.M., Mills, S.K., Hendrickx, J.M.H., Ruiz, J., Chesley, J.T., Asmerom, Y., 2007. Geologic origins of salinization in a semi-arid river: the role of sedimentary basin brines. Geology 35 (12), 1063–1066. https://doi.org/10.1130/G23976A.1.

Hunt, A.G., Darrah, T.H., Poreda, R.J., 2012. Determining the source and genetic fingerprint of natural gases using noble gas geochemistry: a northern Appalachian Basin case study. AAPG Bull. 96 (10), 1785–1811. https://doi.org/10.1306/03161211093.

Johnson, P., Bauer, P., 2012. Hydrogeologic investigation of the Northern Taos Plateau, Taos County, New Mexico. New Mexico Bureau of Geology and Mineral Resources Final Technical Report February 2012 Open File Report 544.

Johnson, P.S., Koning, D.J., Partey, F.K., 2013. Shallow groundwater geochemistry in the Española Basin, Rio Grande rift, New Mexico: evidence for structural control of a deep thermal source. Geol. Soc. Am. Spec. Pap. 494, 261–301. https://doi.org/10.1130/2013.2494(11).

Karlstrom, K.E., Crossey, L.J., Hilton, D.R., Barry, P.H., 2013. Mantle ^{3}He and CO_2 degassing in carbonic and geothermal springs of Colorado and implications for neotectonics of the Rocky Mountains. Geology 41 (4), 495,498. https://doi.org/10.1130/G34007.1.

Kempter, K., Kelley, S., Koning, D., Ferguson, C., Osburn, B., Fluk, L., 2005. Geologic map of the Vallecitos quadrangle, Rio Arriba County, New Mexico. New Mexico Bureau of Geology and Mineral Resources Open-File Geologic map. vol. 108.

Kennedy, B.M., Van Soest, M.C., 2007. Flow of mantle fluids through the ductile lower crust: helium isotope trends. Science 318 (5855), 1433–1436. https://doi.org/10.1126/science.1147537.

Koning, D., Karlstrom, K., Judson, M., Skotnicki, S., Horning, R., Newell, D., Muehlberger, W.R., 2005a. Geologic Map of the Ojo Caliente 7.5 – Minute Quadrangle, Rio Arriba and Taos Counties, New Mexico. New Mexico Bureau of Geology and Mineral Resources New Mexico Tech.

Koning, D., Skotnicki, S., Kelley, S., Moore, J., 2005b. Geologic Map of the Chili 7.5 – Minute Quadrangle. New Mexico Bureau of Geology and Mineral Resources new Mexico Tech.

Koning, D.J., Ferguson, J.F., Paul, P.J., Baldridge, W.S., 2004. Geologic structure of the Veldarde graben and the southern Embudo fault system, north-central. N.M. New Mexico Geological Society, Guidebook 55, 158–171.

Koning, D.J., McIntosh, W., Dunbar, N., 2011. Geology of Southern Black Mesa, Española Basin, New Mexico: New Stratigraphic Age Control and Interpretations of the Southern Embudo Fault System of the Rio Grande Rift. vol. 62. New Mexico Geological Society, Guidebook, pp. 191–214.

Koning, D.J., Grauch, V.J.S., Connell, S.D., Ferguson, J., McIntosh, W., Slate, J.L., Wan, E., Baldridge, W.S., 2013. Structure and tectonic evolution of the eastern Española basin, Rio Grande rift, north-central New Mexico. The Geological Society of America Special Papers 494, 185–219.

Lee, H., Muirhead, J.D., Fischer, T.P., Ebinger, C.J., Kattenhorn, S.A., Sharp, Z.D., Kianji, G., 2016. Massive and prolonged deep carbon emissions associated with continental rifting. Nat. Geosci. https://doi.org/10.1038/ngeo2622.

Lipman, P.W., Mehnert, H.H., 1979. The Taos Plateau volcanic field, northern Rio Grande rift, New Mexico. In: Riecker, R.C. (Ed.), Rio Grande Rift – Tectonics and Magmatism. American Geophysical Union, Washington D.C., pp. 289–312 https://doi.org/10.1029/SP014p0289.

Lupton, J.E., Weiss, R.F., Craig, H., 1977. Mantle helium in Red-Sea brines. Nature 266 (5599), 244–246. https://doi.org/10.1038/266244a0.
Ma, J., Wei, G., Lui, Y., Ren, Z., Xu, Y., Yang, Y., 2013. Precise measurement of stable ($\delta^{88}/^{86}$Sr) and radiogenic (^{87}Sr/^{86}Sr) strontium isotope ratios in geological standard reference materials using MC-ICP-MS. Chin. Sci. Bull. 58 (25), 3111–3118. https://doi.org/10.1007/s11434-013-5803-5.
Magnani, M.B., Miller, K.C., Levander, A., Karlstrom, K., 2004. The Yavapai-Mazatzal boundary: a long-lived tectonic element in the lithosphere of southwestern North America. Geol. Soc. Am. Bull. 116 (9–10), 1137–1142. https://doi.org/10.1130/B25414.1.
Mailloux, B.J., Person, M., Kelley, S., Dunbar, N., Cather, S., Strayer, L., Hudleston, P., 1999. Tectonic controls on the hydrogeology of the Rio Grande Rift, New Mexico. Water Resour. Res. 35 (9), 2641–2659. https://doi.org/10.1029/1999WR900110.
Martin, T.D., Brockhoff, C.A., Creed, J.T., 1994. Determination of Metals and Trace Elements in Water and Wastes Office of Research and Development EPA Method 200.7. vol. 4. US. Environmental Protection Agency, pp. 1–58.
Marty, B., Jambon, A., 1987. C^3 HE in volatile fluxes from the solid Earth: implications for carbon geodynamics. Earth Planet. Sci. Lett. 83 (1–4), 16–26. https://doi.org/10.1016/0012-821X(87)90047-1.
Marty, B., Jambon, A., Sano, Y., 1989. Helium isotopes and CO_2 in volcanic gases of Japan. Chem. Geol. 76 (1–2), 25–40. https://doi.org/10.1016/0009-2541(89)90125-3.
May, J.S., 1984. Miocene stratigraphic relations and problems between the Abiquiú, Los Pinos, and Tesuque Formations near Ojo Caliente, northern Española basin. New Mexico Geological Society Guidebook, 35th Field Conference. Northern New Mexico, Rio Grande Rift.
McGibbon, C., Crossey, L.J., Karlstrom, K.E., Grulke, T., 2018. Carbonic springs as distal manifestations of geothermal system, highlighting the importance of fault pathways and hydrochemical mixing: example from the Jemez Mountains, New Mexico. Appl. Geochem. 98, 45–57. https://doi.org/10.1016/j.apgeochem.2018.08.015.
Miller, J.P., Montgomery, A., Sutherland, P.K., 1963. Geology of Part of the Sangre de Cristo Mountains, New Mexico. New Mexico Bureau of Mines and Mineral Resources, p. 11.
Mills, S.K., 2003. Quantifying Salinization of the Rio Grande Using Environmental Tracers. M.S. Thesis. New Mexico Institute of Mining and Technology.
de Moor, J.M., Fischer, T.P., Sharp, Z.D., Hilton, D.R., Barry, P.H., Mangasini, F., Ramirez, C., 2013. Gas Chemistry and nitrogen isotope compositions of cold mantle gases from Rungwe Volcanic Province, southern Tanzania. Chem. Geol. 339, 30–42. https://doi.org/10.1016/j.chemgeo.2012.08.004.
Moreira, M., Kunz, J., Allegre, C., 1998. Rare gas systematics in popping rock: isotopic and elemental compositions in upper mantle. Science 279, 1178–1181.
Muehlberger, W.R., 1979. The Embudo fault between Pilar and Arroyo Hondo, New Mexico: an active intracontinental transform fault. N. M. Geol. Soc. Guideb. 30, 77–82.
Nereson, A., Stroud, J., Karlstrom, K., Heizler, M., McIntosh, W., 2013. Dynamic topography of the western Great Plains: Geomorphic and ^{40}Ar/^{39}Ar evidence for mantle-driven uplift associated with the Jemez lineament of NE New Mexico and SE Colorado. Geosphere 9 (3), 521–545. https://doi.org/10.1130/GES00837.1.
Newell, D.L., Crossey, L.J., Karlstrom, K.E., Fischer, T.P., 2005. Continental-scale links between the mantle and groundwater systems of the Western Unites States: evidence from travertine springs and regional he isotope data. GSA Today 15 (12), 4–11. https://doi.org/10.1130/1052-5173(2005)015<4:cSlBtM>2.0.CO;2.
Nielson, D.L., Hulen, J.B., 1984. Internal Geology and Evolution of the Redondo Dome, Valles Caldera, New Mexico. University of Utah Research Institute.
Parkhurst, D.L., 1995. User's Guide to PHREEQC – A Computer Program for Speciation, Reaction-Path, Advective-Transport, and Inverse Geochemical Calculations. U.S. Geological Survey Water Resources Investigations Report. 95–4227. p. 143.
Phillips, F.M., Mills, S., Hendrickx, M.H., Hogan, J., 2003. Environmental tracers applied to quantifying causes of salinity in arid-region rivers: results from the Rio Grande Basin, Southwestern USA. Dev. Water Sci. 50, 327–334. https://doi.org/10.1016/S0167-5648(03)80029-1.
Piper, A., 1944. A graphic procedure in the geochemical interpretation of water-analysis. Eos, Transactions American Geophysical Union 25 (6), 914–928. https://doi.org/10.1029/TR025i006p00914.
Polyak, B.G., Tolstikhin, I.N., Kamensky, I.L., Yakovlev, L.E., Marty, B., Cheshko, A.L., 2000. Helium isotopes, tectonics and heat flow in the Northern Caucasus. Geochim. Cosmochim. Acta 64 (11), 1925–1944. https://doi.org/10.1016/S0016-7037(00)00342-2.
Porcelli, D., Ballentine, C.J., 2002. Models for distribution of terrestrial noble gases and evolution of the atmosphere. Rev. Mineral. Geochem. 47 (1), 411–480. https://doi.org/10.2138/rmg.2002.47.11.
Poreda, R., Craig, H., 1989. Helium isotope ratios in circum-Pacific volcanic arcs. Nature 338 (6215), 473–478. https://doi.org/10.1038/338473a0.
Poreda, R.J., Farley, K.A., 1992. Rare gases in Samoan xenoliths. Earth Planet. Sci. Lett. 133 (1), 129–144. https://doi.org/10.1016/0012-821X(92)90215-H.
Poreda, R.J., Craig, H., Arnorsson, S., Welhan, J.A., 1992. Helium isotopes in Icelandic geothermal systems: I. ^{3}He, gas chemistry, and ^{13}C relations. Geochemica et Cosmochimica Acta 56 (12), 4221–4228. https://doi.org/10.1016/0016-7037(92)90262-H.
Poreda, R.J., Schilling, J.G., Craig, H., 1993. Helium isotope ratios in Easter microplate basalts. Earth Planet. Sci. Lett. 119 (3), 319–329. https://doi.org/10.1016/0012-821X(93)90141-U.
Priewisch, A., Crossey, L.J., Karlstrom, K.E., Polyak, V.J., Asmerom, Y., Nereson, A., Ricketts, J.W., 2014. U-series geochronology of large-volume Quaternary travertine deposits of the southeaster Colorado Plateau: evaluating episodicity and tectonic and paleohydrologic controls. Geosphere 10 (2), 401–423. https://doi.org/10.1130/GES00946.1.
Repasch, M., Karlstrom, K., Heizler, M., Pecha, M., 2017. Birth and evolution of the Rio Grande fluvial system in the past 8 Ma: progressive downward integration and the influence of tectonics, volcanism, and climate. Earth-Sci. Rev. 168, 113–164. https://doi.org/10.1016/j.earscirev.2017.03.003.
Robinson, D., Scrimgeour, C.M., 1995. The contribution of plant C to soil CO_2 measured using δ^{13}C. Soil Biology and Biogeochemistry 27 (12), 1653–1656.
Sano, Y., Marty, B., 1995. Origin of carbon in fumarolic gas from island arcs. Chem. Geol. 119 (1), 265–274. https://doi.org/10.1016/0009-2541(94)00097-R.
Sano, Y., Nakamura, Y., Notsu, K., Wakita, H., 1988. Influence of volcanic eruptions on helium isotope ratios in hydrothermal systems induced by volcanic eruptions. Geochim. Cosmochim. Acta 52 (5), 1305–1308. https://doi.org/10.1016/0016-7037(88)90284-0.
Schmandt, B., Humphreys, E., 2010. Complex subduction and small-scale convection revealed by body-wave tomography of the western United States upper mantle. Earth Planet. Sci. Lett. 297 (3), 435–445. https://doi.org/10.1016/j.epsl.2010.06.047.
Sharp, Z., 2007. Principals of Stable Isotope Geochemistry. Upper Saddle River, New Jersey, Prentice Hall, 68-70, 88–89.
Shaw, A.M., Hilton, D.R., Fischer, T.P., Walker, J.A., Alvarado, G.E., 2003. Contrasting He-C relationship in Nicaragua and Costa Rica: insights into C cycling through subduction zones. Earth Planet. Sci. Lett. 214 (3), 499–513. https://doi.org/10.1016/S0012-821X(03)00401-1.
Sherwood Lollar, B., Ballentine, C.J., O'Nions, R.K., 1997. The fate of mantle-derived carbon in a continental sedimentary basin: Integration of C/he relationships and stable isotope signatures. Geochim. Cosmochim. Acta 61 (11), 2295–2307. https://doi.org/10.1016/S0016-7037(97)00083-5.
Snyder, G., Poreda, R., Fehn, U., Hunt, A., 2003. Sources of nitrogen and methane in central American geothermal settings: Noble gas and 129I evidence for crustal and magmatic volatile components. Geochem. Geophys. Geosyst. 4 (1), 1–28. https://doi.org/10.1029/2002GC000363.
Spell, T.L., Kyle, P.R., Baker, J., 1996. Geochronology and Geochemistry of the Cerro Toledo Rhyolite. vol. 47. New Mexico Geological Society. Guidebook, pp. 263–268.
Steck, L.K., Thurber, C.H., Fehler, M.C., Lutter, W.J., Roberts, P., Baldridge, W.S., Stafford, D., Sessions, R., 1998. Crust and upper mantle P wave velocity structure beneath Valles caldera, New Mexico: results from the Jemez teleseismic tomography experiment. Journal of Geophysical Research: Solid Earth 103 (B10), 24301–24320. https://doi.org/10.1029/98JB00750.
Tassi, F., Aguilera, F., Darrah, T., Vaselli, O., Capaccioni, B., Poreda, R.J., Delgato Huertas, A., 2010. Fluid geochemistry of hydrothermal systems in the Arica-Parinacota, Tarapaca and Antofagasta regions (northern Chile). Journal of Volcanolgy and Geothermal Research 192, 1–15. https://doi.org/10.1016/j.jvolgeores.2010.02.006.
Tedesco, D., Tassi, F., Vaselli, O., Poreda, R.J., Darrah, T., Cuoco, E., Yalire, M.M., 2010. Gas isotopic signatures (he, C, and Ar) in the Lake Kivu region (western branch of the East African rift system): Geodynamic and volcanological implications. Journal of Geophysical Research-Solid Earth 115 (B01205), 1–12. https://doi.org/10.1029/2008JB006227.
Tolley, D.G.III, 2014. High-elevation mountain streamflow generation: the role of deep groundwater in the Rio Hondo Watershed, northern New Mexico. New Mexico Institute of Mining and Technology, Master of Science Thesis.
Torres, M.E., Mix, A.C., Rugh, W.D., 2005. Precise δ^{13}C analysis of dissolved inorganic carbon in natural waters using automated headspace sampling and continuous-flow mass spectrometry. Limnol. Oceanogr. Methods 3, 349–360.
Truesdell, A.H., Janik, C.J., 1986. Reservoir processes and fluid origins in the Baca Geothermal System, Valles Caldera, New Mexico. Journal of Geophysical Research: Solid Earth. 91 (B2), 1817–1833. https://doi.org/10.1029/JB091iB02p01817.
Vuataz, F., Stix, J., Goff, F., Pearson, C.F., 1984. Low-Temperature Geothermal Potential of the Ojo Caliente Warm Springs Area, Northern New Mexico. Los Alamos National Laboratory https://doi.org/10.2172/6771133.
Vuataz, F.D., Goff, F., Fouillac, C., Calvez, J.Y., 1988. A strontium isotope study of the VC-1 core hole and associated hydrothermal fluids and rocks from Valles Caldera, Jemez Mountains, New Mexico. Journal of Geophysical Research: Solid Earth. 93 (B6), 6059–6067. https://doi.org/10.1029/JB093iB06p06059.
Weiss, R., 1971a. The effect of salinity on the solubility of argon in water and seawater. Deep-Sea Res. Oceanogr. Abstr. 18 (2), 225–230. https://doi.org/10.1016/0011-7471(71)90111-2.
Weiss, R., 1971b. Solubility of helium and neon in water and seawater. Journal of Chemical and Engineering Data 16 (2), 235–241. https://doi.org/10.1021/je60049a019.
Welhan, J.A., 1988. Origins of methane in hydrothermal systems. Chem. Geol. 71 (1), 183–198. https://doi.org/10.1016/0009-2541(88)90114-3.
White, A.F., Delany, J.M., Truesdell, A., Janik, K., Goff, F., Crecraft, H., 1984. Fluid Chemistry of the Baca Geothermal Field, Valles Caldera, New Mexico. vol. 35. New Mexico Geological Society, Guidebook, pp. 257–263.
Williams, A.J., Crossey, L.J., Karlstrom, K.E., Newell, D., Person, M., Woolsey, E., 2013. Hydrogeochemistry of the Middle Rio Grande aquifer system – Fluid mixing and salinization of the Rio Grande due to fault inputs. Chem. Geol. 351, 281–298. https://doi.org/10.1016/j.chemgeo.2013.05.029.
Zimmerer, M.J., Lafferty, J., Coblec, M.A., 2016. The eruptive and magmatic history of the youngest pulse of volcanism at the Valles caldera: Implications for successfully dating late Quaternary eruptions. J. Volcanol. Geotherm. Res. 310, 50–57. https://doi.org/10.1016/j.jvolgeores.2015.11.021.